Departamento de Ingeniería
Química y Tecnologías
del Medio Ambiente
Universidad Zaragoza

MASTER DEGREE IN NANOSTRUCTURED MATERIALS FOR NANOTECHNOLOGY APPLICATIONS 2011-2013

Final Master Project

SYNTHESIS AND CHARACTERIZATION OF GRAPHENE OXIDE AND REDUCED GRAPHENE OXIDE AND ITS USE IN FLEXIBLE PHOTOVOLTAIC CELLS

Autor: Mikel Hurtado

Advisor: Dr. Joaquín Coronas

Universidad de Zaragoza

Instituto de Nanociencia de Aragón (INA)

January 28th 2013

Table of contents

Objectives

1. **Synthesis of GO and RGO:** Graphene oxide obtaining by exhaustive oxidative reaction of fine Carbon particles. Obtained GO is reduced in order to produce the reduced graphene oxide (OGR) and design GO and RGO stabilized suspensions.

2. **Characterization of OG and OGR:** Techniques like X-ray diffraction XRD, FTIR, UV-vis absorption spectroscopy, SEM, TEM and TGA give information about crystallographic structure, functional groups, electronic transitions, morphology, grade of exfoliation, and thermal degradation as function of temperature respectively.

3. **Photovoltaic solar cell design:** Design and build up of photovoltaic device substrate/TiO_2/Dye/(I_2/I_3^-)/CounterElectrode/substrate type, substrates can be of soda lime glass SLG or PET, the counter electrodes are de synthesized materials GO and RGO, and the dye is Tris (2,2´ bipyridyl dichlororuthenium (II)), being I_2/I_3^- the pair redox.

4. **I-V characteristic curve:** Study of photovoltaic performance parameters under illumination standard conditions for flexible solar cell devices based on GO and RGO.

1. Motivation

Carbon materials have important roles currently both industrially and domestically. The pencils are made of graphite. Black ink based carbon is used to print on paper. The lithium cell phone´s operates with lithium intercalated into carbon electrodes. Several sport equipment are made around carbon/carbon fiber composites and a modern airplanes have structural components made of carbon/carbon fiber systems. Steel industry uses High purity graphite electrodes. The aluminum industry use carbon anodes, made from delayed cokes from petroleum. Part of nuclear energy generation is based on neutron graphite moderated systems. Microporous carbons, with their high adsorption capacities, have important purification roles. Metallurgical coke, from coal, is required to steel and iron manufacture. Carbon is highly used and highly investigated material that has several applications, and it depends dramatically of its particular carbon structure [1].

Taking in to account nowadays carbon importance, the main motivation of this Master project is try to improve the graphene synthesis by chemical methods in order to have reproducible and robust procedure to obtain graphene sheets (Graphene Oxide and Reduced Graphene Oxide). We will use the knowledge related to solid state chemistry, semiconducting materials and photovoltaic to prove our materials as efficient nanomaterials for optoelectronic applications in Grätzel-type flexible solar cell devices.

2. Introduction

Carbon is ancient but at the same time new material. It has been used for centuries going back to antiquity, but yet many new crystalline forms of carbon have only recently been experimentally discovered in the last few decades. These newer crystalline forms include buckyballs, carbon nanotubes (CNTs), and graphene, as shown in Figure 1.

These structures share in common a hexagonal lattice or arrangement of carbon atoms. In addition, CNTs and graphene occupy a reduced amount of space compared with their older known structures; hence, they are often referred to as reduced-dimensional or low-dimensional solids being very investigated nowadays in nanoscience. To give a comparative idea of the critical size scales of these nanomaterials, nanotubes are about 10 000 times thinner than human hair, and graphene is about 300 000 times thinner than a sheet of paper. The typical diameter of nanotubes range from about 1 to 100 nm, and graphene ideally has the thickness of a single atomic layer ($<$3.4 Å). Fundamentally, it is the combination of the reduced dimensions and the different lattice structure that leads to the fascinating properties unique to nanotubes and graphene [2].

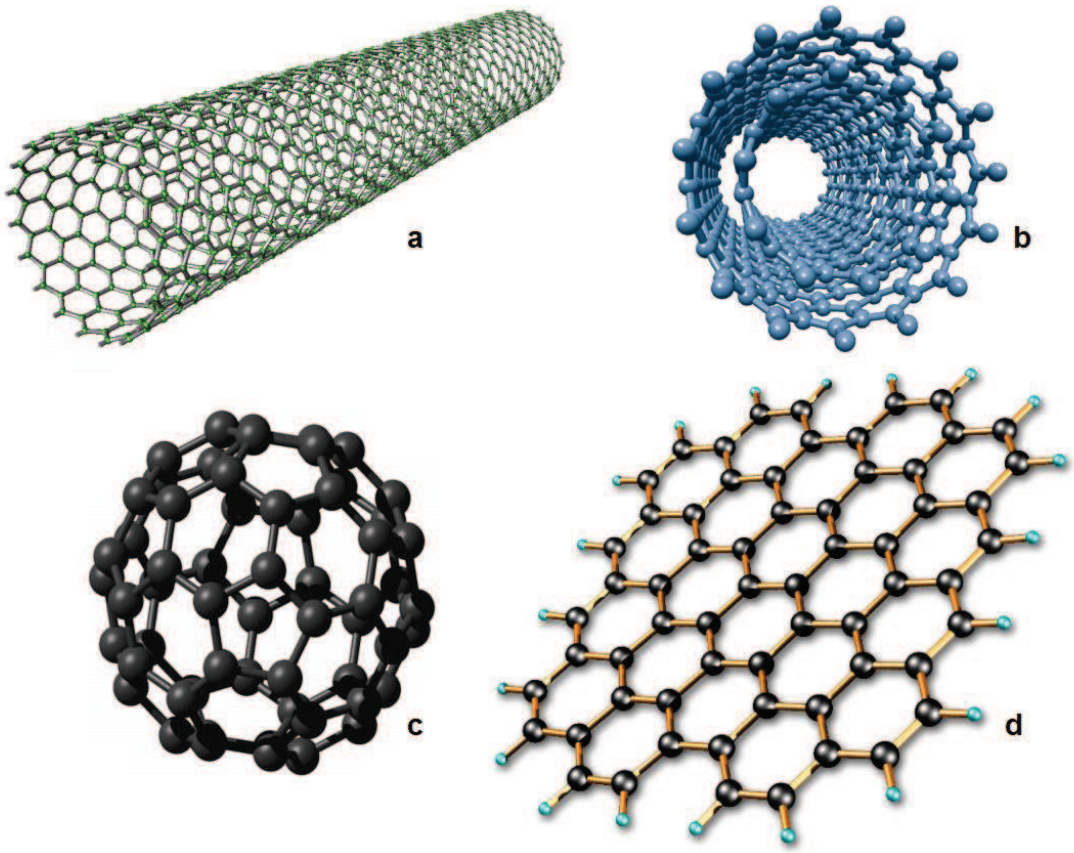

Figure 1. Different Carbon structures a) Single Wall Carbon Nanotube SWCNT, b) Multi Wall Carbon Nanotube MWCNT, c) Fullerene and d) Graphene or single graphite sheet.

In words of Geim and Novoselov: “Unrolling an open SWCNT into a flat sheet gives graphene – a chicken wire mesh of carbon atoms that is a single atom thick”. Graphene is very difficult to isolate because it tends to curl up, but in 2004 André Geim’s group in Manchester, UK, found a method of isolating individual graphene flakes by simply cleaving graphite with sticky tape. As a nanomaterial graphene has tremendous potential. Its defect-free structure makes it an extremely effective electrical conductor which, coupled with its small size, holds out great promise for a new generation of computer chips and microelectronic devices.

Applications in other areas such as batteries, solar cell coatings and LCD displays have taken very relevance. Lithographic etching of such a thin material is extremely challenging, although use of extremely thin (5–10 nm wide) strips may aid the process, however, the first graphene transistors have already been produced either based on an electric field used to control current flow through a graphene sheet or by surrounding a graphene quantum dot with two graphene sheets to restrict the passage of electrons (Figure 2). One problem with graphene is that it is such a good conductor that leakage of current through such devices can occur even when the device is supposed to be off [3].

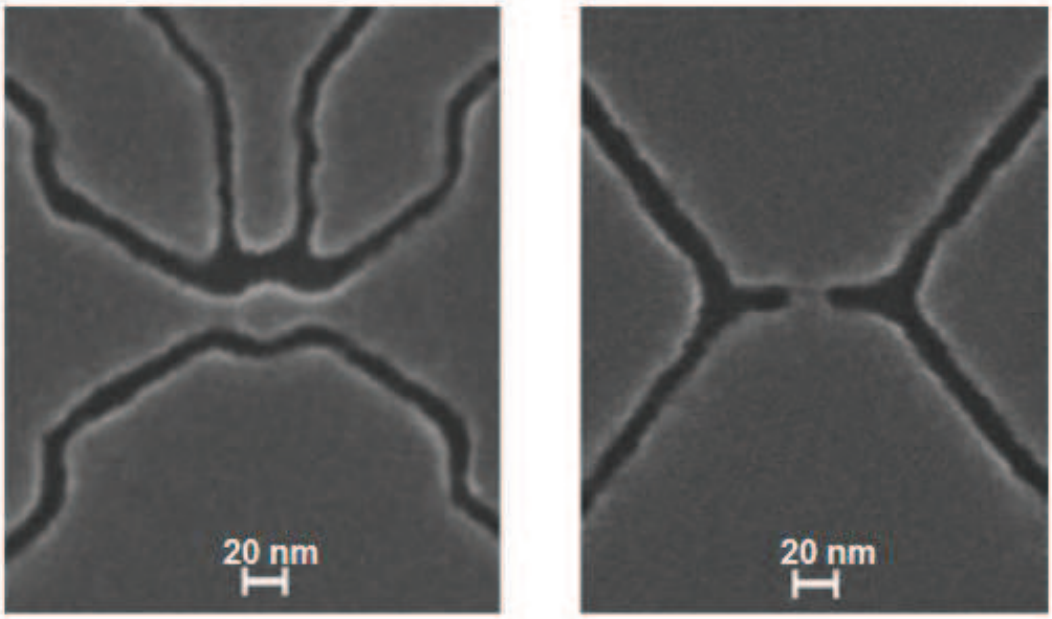

Figure 2. SEM image of: (a) a graphene quantum dot device, and (b) a nanoconstriction [2].

3. Graphene

Graphene is a single layer of sp^2-bonded carbon which can be seen as an individual atomic plane of bulk graphite. The interest in graphene is driven by the high crystal quality and ballistic transport at sub-micron distances as well as the behavior of quasi-particles as massless Dirac fermions so that the electronic properties are governed by quantum electrodynamics rather than the standard physics of metals based on the (non-relativistic) Schrödinger equation [4 - 5].

Graphene up to sizes of 100 μm can be obtained by micromechanical cleavage of bulk graphite [6] although graphene crystallites left on a substrate are extremely rare [7, 8, 9]. Peierls [10] and Landau [11] predicted that strictly 2D crystals were thermodynamically unstable and could not exist because a divergent contribution of thermal fluctuations in low-dimensional crystals should lead to such large displacements of atoms that they become comparable to interatomic distances and dislocations should appear in 2D crystals [12] at any finite temperature. However, strong interatomic bonds can ensure that thermal fluctuations cannot lead to the generation of dislocations [13] and 2D crystals are intrinsically stabilized by soft crumpling in the third dimension [14]. Figure 3 shows different carbon based schemes bands.

For becoming large-scale graphene applications, two requirements are of importance:

- Suitable synthesis of larger graphene amounts.
- Pattering Control, morphology, and crystallinity of the graphene edges nano-sheets, because these can exhibit either semi-metallic or semiconducting behavior [15, 16].

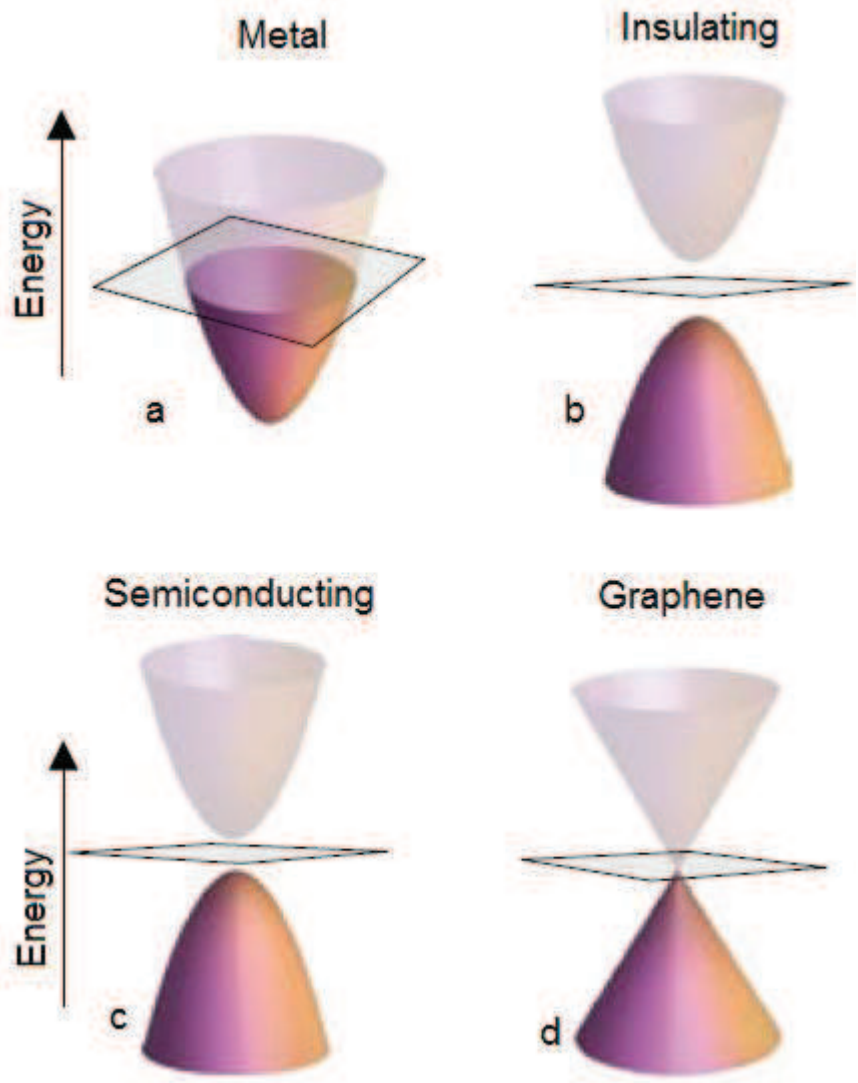

Figure 3. Schemes bands of a) metal bands, b) insulating bands, c) semiconducting bands and d) graphene bands [4, 7].

Graphene is an atomic carbon monolayer densely packed into a 2D honeycomb lattice and it is the building block for graphitic materials of all other dimensionalities. Graphene exhibits physical properties at the interface between traditional condensed matter physics and the theory of relativistic electrons in vacuum–quantum electrodynamics (QED) [5, 7, 18, 19] having relevant importance due to its high-charge carrier mobility at room temperature, its band gap control and potential for many-body-correlated effects [20]. Chemically synthesized graphene appears to be available in sufficient quantities [21] with a wide range of applications [17], including nano-composites, electronic devices, solar cells, fuel cells, sensors and catalysis.

3.1. Electronic Structure

The electronic structure of graphene follows from a nearest-neighbor tight-binding approximation calculation [5, 14, 17, 23, 29]. The two atoms per graphene unit cell and hence the two graphene sub-lattices give rise to two "conical" points per Brillouin zone where band crossing occurs, *K* and *K´* (Figure. 4), and where the electron energy $\mathbf{E} = \hbar\mathbf{k}V_F$ is linearly dependent on the wave vector **k** with the Fermi velocity $\boldsymbol{V}_F = c/300$. What makes graphene so interesting is that the energy spectrum closely resembles the energy spectrum derived from the Dirac equation for massless relativistic fermions, such as electrons [24].

For Dirac particles with the mass *m*, the energy $\mathbf{E} = c\hbar\mathbf{k}$ is linearly dependent on the wave vector **k** when $E >> E_0 = mc^2$ and for *massless* Dirac fermions the gap between the electron and the positron energy is zero. Then, the graphene electrons may be used for studying the properties of these massless Dirac particles where the role of the speed of light is played by the Fermi velocity. Because of the linear energy spectrum, one can expect that quasi particles in graphene behave differently from those in conventional metals and semiconductors with a parabolic (free electron-like) dispersion relation.

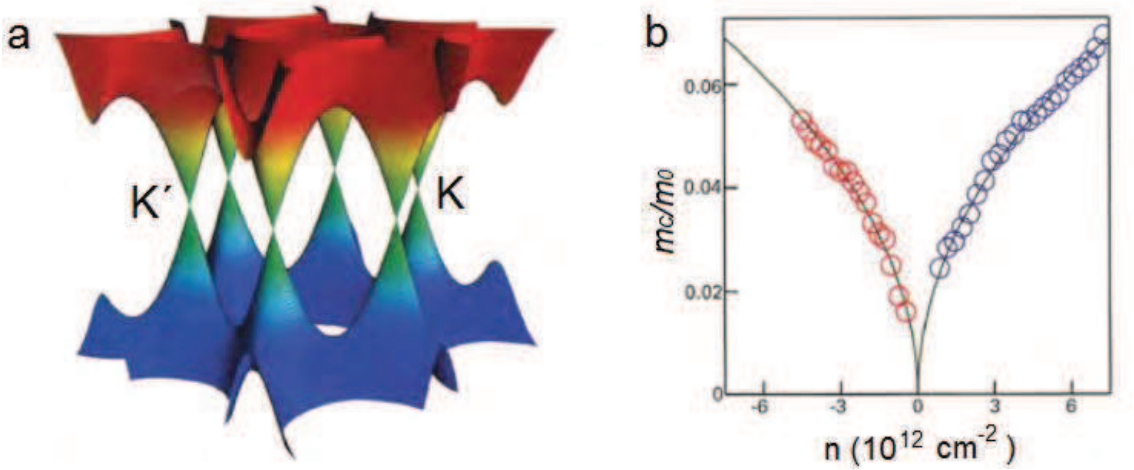

Figure 4. a) Band structure of graphene. The conduction band touches the valence band at the K and K´points [7]. b) Electron and hole cyclotron masses as a function of carrier concentration in graphene. The square-root dependence suggests a linear dispersion relation [4].

Above zero energy the current-carrying states in graphene are, as usual, electron like and negatively charged. At negative energies, if the valence band is not full, unoccupied electronic states behave as positively charged holes. However, in contrast to electrons and holes in solid-state physics described by different Schrödinger equations and different effective masses, holes and electrons in graphene should be interconnected in analogy to the charge-conjugation (electron–positron) symmetry in quantum electrodynamics (QED) [24 - 29].

Due to the exceptional electronic quality of graphene the electron and hole concentrations ***n*** can be as high as $10^{13}/cm^2$, mobility $\boldsymbol{\mu}$ can exceed 15000 cm^2/Vs even under ambient conditions [6] and may be improved to 100000 cm^2/Vs [28]. This demonstrates ballistic charge carrier transport up to 300 nm at

300 K. A further indication of the system's high electronic quality is the quantum Hall effect (QHE) that can be observed in graphene even at room temperature [30 - 31]. For zigzag graphene nano-sheets magnetic ordering has been found at the edges and by first principle simulations [32] for spin-valve devices, magneto-resistance values have been predicted that are thousand times higher than previously reported experimental values. The thermoelectric power of graphene is gate dependent [33]. Confinement gaps up to 0.5 eV for semiconducting behavior can be opened in graphene by nano-sheets patterning employing scanning tunneling microscope (STM) lithography [34 - 37].

3.2. Quantum Hall Effect

Magneto-oscillation effects as the de Haas–van Alphen or the Shubnikov–de Haas effects are the most reliable tools to investigate electron-energy spectra in metals and semiconductors [38]. In a 2D system with a magnetic field *B* perpendicular to the system's plane, the energy spectrum is discrete (Landau quantization). In the case of massless Dirac fermions the energy spectrum yields the form:

$$E_{\nu\sigma} = \pm\sqrt{2\,|e|\,B\hbar v_{\mathrm{F}}^2\,(\nu + 1/2 \pm 1/2)}$$

where ***v*** is the quantum number and the term ±1/2 is connected with the chirality [7]. By varying ***B*** at a given electron concentration ***n*** one can tune the Fermi energy $\boldsymbol{E_F}$ to coincide with one of the Landau levels. This drastically changes the properties of the solid and various properties will oscillate with 1/*B*. From the amplitude of the oscillations the effective cyclotron mass of the charge carriers can be derived. For massless Dirac fermions this quantity should be proportional to $\boldsymbol{n}^{1/2}$, which is exactly the behavior found experimentally [4, 8] (see Fig. 4b).

For two carbon layers a gapless state with *parabolic* bands touching at the *K* and *K´* points are predicted instead of conical bands [39] so that bilayer graphene can be treated as a gapless semiconductor. The energy states in a *B* field are given by:

$$E_\nu \propto \sqrt{\nu\,(\nu - 1)}$$

and, thus, the number of zero energy states (v = 0 and v = 1) is twice that of monolayer graphene. Therefore, the QHE in bilayer graphene differs from both single-layer graphene and conventional semiconductors [40 - 42]. In the other hand, potential graphene barriers are rather transparent. Therefore, different electron and hole puddles induced by disorder are not isolated but percolate effectively, thereby suppressing localization. This is important for understanding the minimum conductivity = *e2/h* observed experimentally in graphene [4, 41, 40, 42].

3.3. Graphene Devices

Nanometer scale graphene structures show high-quality transistor action. Best candidates for graphene-based FETs will be devices based on quantum dots and devices using *p*–*n* junctions in bilayer graphene [7]. Negligible spin–orbit coupling makes the spin polarization in graphene to survive over sub-micrometer distances yielding applications in spintronics. Superconductivity can be induced through the proximity effect and the supercurrent can be controlled by an external gate voltage giving prospects for usage in superconductive FETs [7]. The sensitivity of the graphene electrical resistivity to the absorption of gases may be employed for sensor operation [7]. Also their surface resistance properties can be used as transparent conducting electrodes and several modern flexible devices, being this application one of the main objectives of this Master project.

3.4. Hybridization and some other properties

Carbon is a very active element in producing many molecular compounds and crystalline solids. Carbon has four valence electrons, which tend to interact with each other to produce the multiple types of carbon allotrope.

In elemental form, the four valence electrons occupy the ***2s*** and ***2p*** orbitals, as illustrated in Figure 5a. When carbon atoms come together to form a crystal, one of the ***2s*** electrons is excited to the ***2p$_z$*** orbital from energy gained from neighboring nuclei, which has the net effect of lowering the overall energy of the system. Giving way to the interactions or bonding subsequently follows between the ***2s*** and ***2p*** orbitals of neighboring carbon atoms. In chemistry, these interactions or mixing of atomic orbitals is commonly called hybridization, and the new orbitals that are formed are referred to as hybrid orbitals (Figure 5c).

The existence of multiple types of hybridization in carbon is what leads to the different allotropes shown in Table 1. Graphene is a planar allotrope of carbon where all the carbon atoms form covalent bonds in a single plane. The planar honeycomb structure of graphene has been observed experimentally and is shown in Figure 6. Graphene can be considered the mother of three carbon allotropes [2].

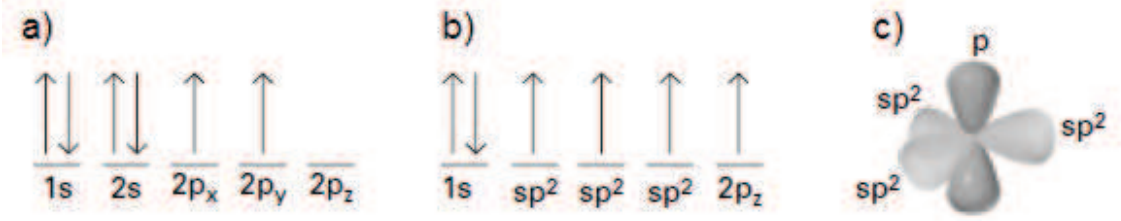

Figure 5. The arrangement of electrons and their relative spin in (a) elemental carbon and (b) graphene. (b) The s and two of the p orbitals of the second shell interact covalently to form three sp^2 hybrid orbitals. (c) Illustration of the orbitals.

Dimension	0D	1D	2D	3D
Allotrope	C60 buckyball	Carbon nanotubes	Graphene	Graphite
Structure	Spherical	Cylindrical	Planar	Stacked planar
Hybridization	sp^2	sp^2	sp^2	sp^2
Electronic properties	Semiconductor	Metal or semiconductor	Semi-metal	Metal

Table 1. Allotropes of graphene

Stacking several sheets of graphene leads to graphite, wrapping graphene into a sphere produces Fullerenes and folding into a cylinder produces nanotubes as we can saw in (Figure 1).

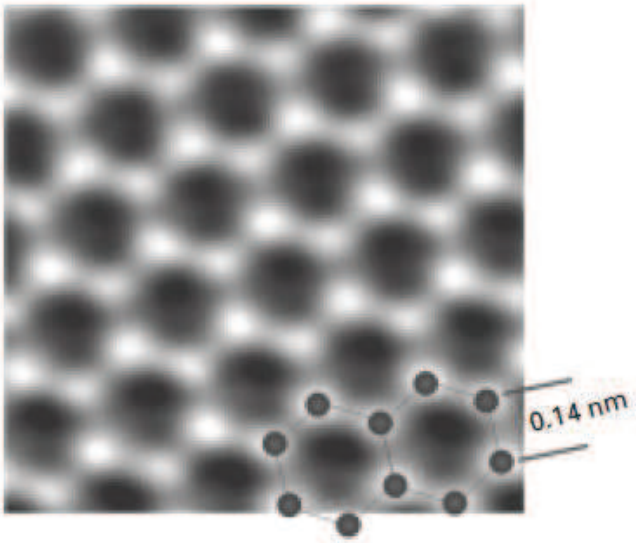

Figure 6. Remarkable transmission electron aberration-corrected microscope (TEAM) image of graphene vividly showing the carbon atoms and bonds in the honeycomb structure (courtesy of Berkeley's TEAM05, 2009) [2]

In graphene, the ***2s*** orbital interacts with the $\boldsymbol{2p_x}$ and $\boldsymbol{2p_y}$ orbitals to form three $\boldsymbol{sp^2}$ hybrid orbitals with the electron arrangement (Figure 5b). The $\boldsymbol{sp^2}$ interactions result in three bonds called σ-bonds, which are the strongest type of covalent bond. The σ-bonds have the electrons localized along the plane connecting carbon atoms and are responsible for the great strength and mechanical properties of graphene and CNTs. The $\boldsymbol{2p_z}$ electrons form covalent bonds called π-bonds, where the electron cloud is distributed normal to the plane connecting carbon atoms. The $\boldsymbol{2p_z}$ electrons are weakly bound to the nuclei and, hence, are relatively delocalized. These delocalized electrons are the ones responsible for the electronic properties of graphene and CNTs. Table 2 shows the most important physical graphene properties

Properties	Value	Observations	Ref
Length of the lattice vector	$a = (3)^{1/2}a_{C-C}$	a_{C-C} =1.42 Å is the carbon bond length	[19]
Surface area	2600 m^2g^{-1}	theoretical prediction	[43]
Mobility	15000 $cm^2 V^{-1} s^{-1}$ (typical) 200000 $cm^2V^{-1} s^{-1}$ (intrinsic)	room temperature	[44] [4] [6] [7]
Means free path (ballistic transport)	300–500 nm	room temperature	[45]
Fermi velocity	c/300=1000000 ms^{-1}	room temperature	[45]
Electron effective mass	0.06 m_o	room temperature	[45]
Hole effective mass	0.03 m_o	room temperature	[45]
Thermal conductivity	$(5.3\pm0.48)x10^3$ WmK^{-1}	better thermal conductivity than in most crystals	[46]
Breaking strength	40 Nm^{-1}	reaching theoretical limit	[47]
Young modulus	1.0 TPa	ten times greater than in steel	[47]
Opacity	2.3%	visible light	[48]
Optical transparency	97.7%	visible light	[48]

Table 2. Important physical properties of graphene.

4. Graphene Oxide

Graphene-derived materials are of interest among other reasons due to the excellent properties that the graphene sheet has. An important challenge involves developing homogeneous colloidal suspensions of individual graphene sheets by scalable synthesis methods to accelerate the use of such colloidal suspensions, including on large scale [49].

The graphite oxide or graphite derivatives have been used as a starting material in the production of colloidal suspensions of thin platelets. While graphene oxide that is obtained by graphene oxides reduced by chemical [50- 55], thermal [56, 57] and UV-assisted [52] approaches have been shown to be electrically conductive and hold promise in various applications, while graphene oxide that is obtained by simple sonication of graphite oxide is electrically insulating. Graphene sheets are hydrophobic and readily agglomerate in hydrophilic solvents and evidently in solvents that do not have the right range of cohesive energies [54]. Consequently, production of a homogeneous colloidal suspension of electrically conductive graphene sheets in solvents allowing their broad use for both fundamental study and in new technological applications.

5. Renewable energy, solar cells and graphene

Nowadays, World energy consumption is estimated in 13 (TW) terawatts with an expectation of 30 (TW) in 2050 [58]. Then, CO_2 emissions going to be greater almost three times, also the accumulation in the atmosphere would be more twice than today, giving rises the global warming. Supply these energy requirements without using fossil derived and petroleum products is a challenge to not causes environmental damages, in this way renewable energies becoming currently a good alternative in order to use better the natural resources. When we are talking about renewable energies, solar technology occupied the first place due to the energy that comes from the sun is permanent, and also is the cleanest energy that humans have known ever. However the efficiency and materials demand and exploitation are very expensive compared with fossil fuels. Thereby, the amount of produced annual energy by solar cell devices is growing up, driven for the new environmental policies related with contaminant emissions and radioactive dispose substances [59-61].

Most of the currently solar cell devices are fabricated with silicon mono and polycrystalline. Silicon technology has a drawback which is related with the indirect ban-gap, having a certain optimal thickness required to be fabricated, factor that increases the production prices. The second generation of solar cell devices, is known as thin film technology, mainly Silicon in fine layers and semiconducting compounds based on Cooper systems $CuInS_2$, $CuInSe_2$ or more complex systems like $Cu(In,Ga)(S,Se)_2$ [62 -66]. Thin film technology drawbacks are related with the use of heavy metals such as Cd, Te and Se in their both buffer and absorbent layers, and also, by the use of rare materials like Indium and Gallium.

One third new generation of solar cells is based on the fact to produce multi-junctions with the main objective to increase efficiency, also concepts like inter-media band gap, hot carriers, quantum dots, nanocomposites and organic based solar cells are being investigated [67]. However, nanometer scale materials are being used to resolve some problems for example DSSC (Dye Sensitized Solar Cells) have connections based on carbon nanotubes (1D material) in the TiO_2 electrodes. However, the efficiency is limited between TiO_2 nanosphere and its junction with the carbon nanotubes. But when is used graphene (2D materials) instead of carbon nanotubes, the electrical connection between TiO_2 nanoparticles could do multiple buildings with the graphene surface. That means, that the recombination charge processes is decreased due to the acceleration electron generated in the TiO_2 conduction band (thanks to the excellent electrical conduction of graphene [68]). Also, graphene shows high transparence and can be assembled in an electrode having film shape or thin film feature, property that can be used in solar cell devices like in this final master project, due to its catalytic property that allows the reduction process of I_2 to I^-.

5.1. Graphene as transparent conducting oxide in solar cell devices

A critical aspect in solar cell devices is the use of transparent conducting oxides (TCO) such as tin doped indium oxide (ITO) and fluoride doped tin oxide (FTO), these materials allow current flux due to their high conductance.
Nevertheless, ITO and FTO have some drawbacks:

- ITO and FTO are made of rare elements.
- Have ion diffusion from ITO or FTO to the organic polymer layer, reducing the device efficiency.
- Low transparence in the near infrared zone.
- ITO is unstable in acid and basic media.
- ITO and FTO are highly fragile limiting their application in flexible devices.

Carbon nanotubes have been used but their conductivity versus its transparency show worst results that viewed with ITO [69 - 72]. Further, carbon nanotubes have high roughness and agglomeration effects, limiting its use due to high production costs.
Graphene looks like ideal and alternative 2D material to be used in solar modules due to its self-assembly capability as transparent working electrode in thin film with a extremely flat surface, having thickness around carbon mono atomic scale (high transparency both in visible and infrared range) and low preparation costs. [73, 74].

6. Experimental

Graphene oxide (GO) and reduced graphene oxide (RGO) were characterized structural, morphologic and chemically by different techniques at different conditions. In addition photovoltaic parameters were determined for GO and RGO in a Grätzel DSSC device by standard illumination conditions through I-V characteristic response.

Scanning Electron Microscopy (SEM): This morphological characterization technique was used to observe the morphology of the particles and the homogeneous dispersion of the materials on the substrates and composites films. It is based on the sample scanning with a highly energetic beam of electrons. The emitted electrons from the sample surface are the main signal that the detector collects. A sample topographic image is obtained due to low energetic electrons or to secondary and retrodispersed electrons. The samples must be previously covered by a gold thin film since the sample must be conducting. The microscope used, JEOL JSM 6400, belongs also to the University of Zaragoza and Aragon Nanoscience Institute (LMA-INA).

Other image characterization was carried out by transmission electron microscopy (TEM, with a JEOL-2000 FXII microscope from the University of

Zaragoza) is used in this case to measure the interlayer spacing and to observe the interaction of the each carbon monolayer. Also a selected area electron diffraction probe (SAED) was used to determine crystalline properties of the synthesized carbon layers.

Thermogravimetric analysis is a type of testing that determines changes in weight in relation to a temperature program in a controlled atmosphere using a precision thermo balance. A derivative weight loss curve can identify the point where weight loss is most apparent. When temperature is high enough to decompose components into a gas is possible to determine the mass percentage of each impurity in a certain mixture, given an idea of inorganic and organic moieties and also about the interaction between them. The experimental analysis was carried out in a thermogravimetric equipment DSC 822^e Mettler Toledo (equipment of Chemical Engineering Department, University of Zaragoza) with a temperature program of 5ºC/min between 25 to 900 ºC in a controlled air flux atmosphere.

FTIR (Fourier Transform Infrared Spectroscopy) was used to determine functional groups and many vibrational modes corresponding to different moieties. IR Affinity-1 Shimatzu equipment has an internal single beam standard optics system, High-energy ceramic light source, wavenumber range 4000 to 500 cm^{-1}, mirror speed 2.0 mm/s and DLATGS detector with temperature control mechanism. The accuracy of the equipment is 4 cm^{-1}. In FTIR spectroscopy Infrared light is guided through an interferometer and then through the sample (or vice versa). A moving mirror inside the equipment changes the distribution of infrared light that passes through the interferometer. The signal directly recorded, called an "interferogram", represents light output as a function of mirror position.

UV-VIS spectra were achieved in V670 Jasco spectrophotometer from Analytical Instruments using double-beam, single monochromator design covering a wavelength range 190 to 2700 nm. The V-670 double-beam spectrophotometer utilizes a unique, single monochromator design covering a wavelength range from 190 to 2700 nm. A PMT detector is provided for the UV/VIS region and a Peltier-cooled PbS detector is employed for the NIR region. Both gratings and detector are automatically exchanged within the user selectable 800 to 900 nm range. Deuterium lamp range of 190 to 350 nm and halogen lamp range of 330 to 2700 nm. UV-VIS refers to absorption spectroscopy or reflectance spectroscopy in the ultraviolet-visible spectral region. This means it uses light in the visible and adjacent (near-UV and near-infrared (NIR)) ranges. The absorption or reflectance in the visible range directly affects the perceived color of the chemicals involved. In this region of the electromagnetic spectrum, molecules undergo electronic transitions. This technique is complementary to fluorescence spectroscopy, in that fluorescence deals with transitions from the excited state to the ground state, while absorption measures transitions from the ground state to the excited state. Molecules containing π-electrons or non-bonding electrons (n-electrons) can absorb the energy in the form of ultraviolet or visible light to excite these electrons to higher anti-bonding molecular orbitals. The more easily excited the

electrons (i.e. lower energy gap between the HOMO and the LUMO), the longer the wavelength of light it can absorb.

Structural characterization was carried out by X-ray diffraction (XRD), giving information related with crystallographic phases or mix of them. It consists of the application of a collimated X-ray incident beam which is scattered by crystalline phases and represented in a diffractogram as the number of counts received by the detector versus the scattered angle. In this case, they were carried out with D-Max Rigaku X-ray diffractometer, from the University of Zaragoza, with a copper anode and a graphite monochromator to select CuKα radiation, with λ= 1.5418 Å, being the angles interval from 2.5º to 40º with a speed of 0.03º/s.

6.1. Synthesis of graphene oxide (GO) and graphene reduced oxide (GRO)

6.1.1. Graphite exfoliation

Graphene sheets exfoliation were prepared using an exhaustive oxidation process or Hummers process [75, 76]. We have used two commercial materials: highly milled carbon graphite type particles UF4 (large flake particles of 10 micrometers average size from GK company Graphit Kropfmuehl) and ball milling carbon graphite GR5 of 5 micrometers average size. Other carbon particles were used but the most relevant results were carried out by UF4 and GR5.

Graphite particles (0.5 g) were mixed with $NaNO_3$ (0.375 g). Sulfuric acid 5 wt% (37.5 mL) was slowly added to the previous mixture. A cooled bath was required because the process is highly exothermic. After, $KMnO_4$ (2,25 g) was slowly added during 30 min, and the resulting suspension was maintained at 96 ºC under stirring during 2 hours. Keeping temperature at 60 ºC H_2O_2 30 wt% (6 mL) was added and the stirring continued for 2 hours more.

In order to remove both ions and impurities becoming from the oxidation process, 200 mL of H_2SO_4 3 wt% and H_2O_2 0.5 wt% were used to clean the resulting particles by several ultrasound assisted washings. The process was repeated once using water. The resulting products were named GO UF4 and GO GR5 (figure 7). This graphene oxide (GO) is suitable to produce suspensions.

6.1.2. GO suspensions

GO aqueous suspensions of 6 mg/mL concentration were prepared with both GO UF4 and GO GR5 particles. These suspensions were left under stirring at room temperature; during 2 h. Water has been shown as better solvent media than acetone, toluene, ethanol and methanol after several essays.

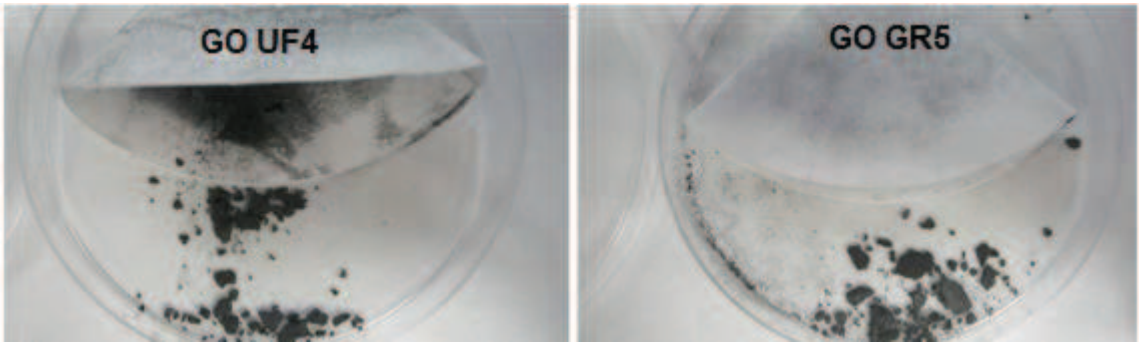

Figure 7. Samples GO UF4 and GO GR 5.

Figure 8, shows the resulting GO UF4 and GO GR5 water suspensions. These suspensions are very stable and do not experience evident agglomeration or fast precipitation. The energy given to the system during stirring process is high enough to increase the particle solvation.

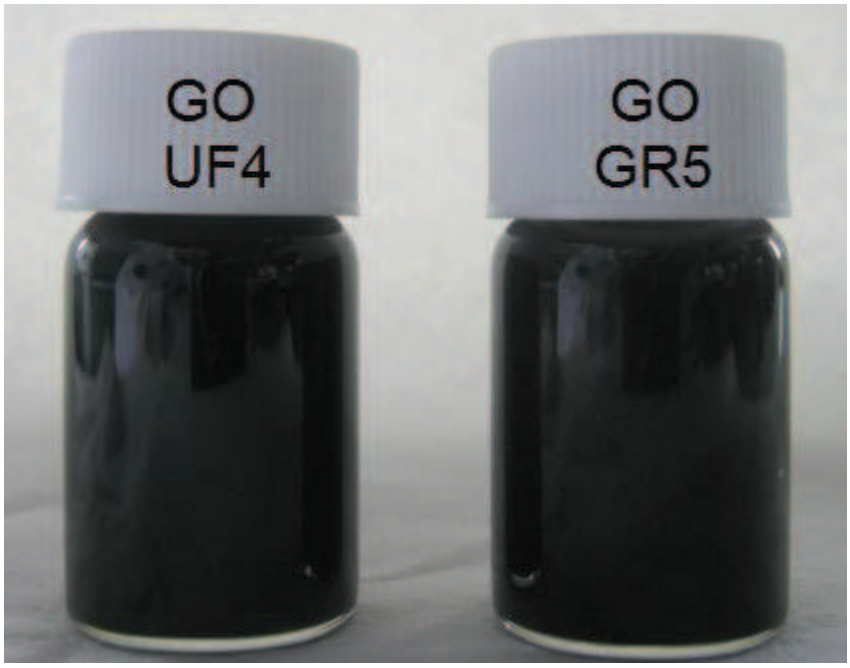

Figure 8. GO UF4 and GO GR 5 suspensions

6.1.3. GO thin films

Both GO UF4 and GO GR5 were used to produce thin films starting from the suspensions above mentioned. The coating process was carried out on glass and PET substrates.

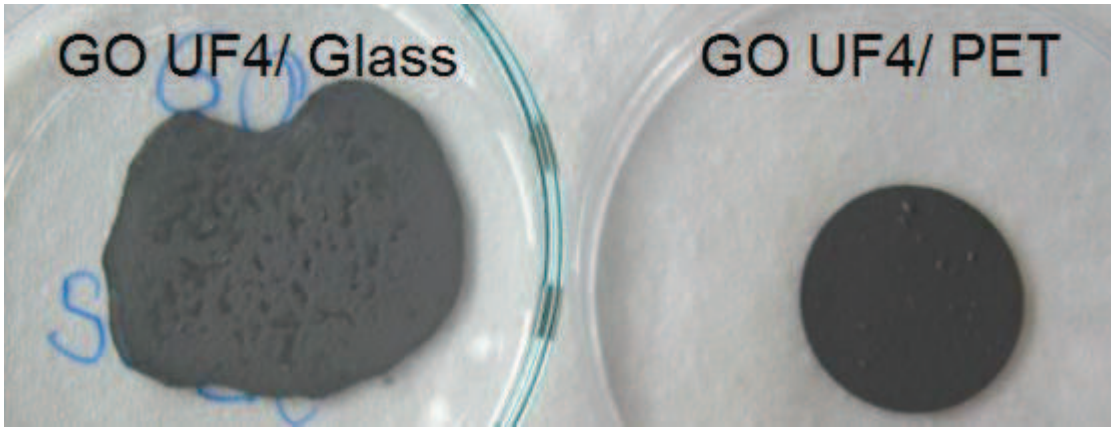

Figure 9. Thin films of GO UF4 both on glass and on PET.

Both sample are forming thin films, once the solvent has been evaporated at room temperature (figure 9). Sample GO UF4 is more homogeneous spread on PET substrate but on glass has largest area.

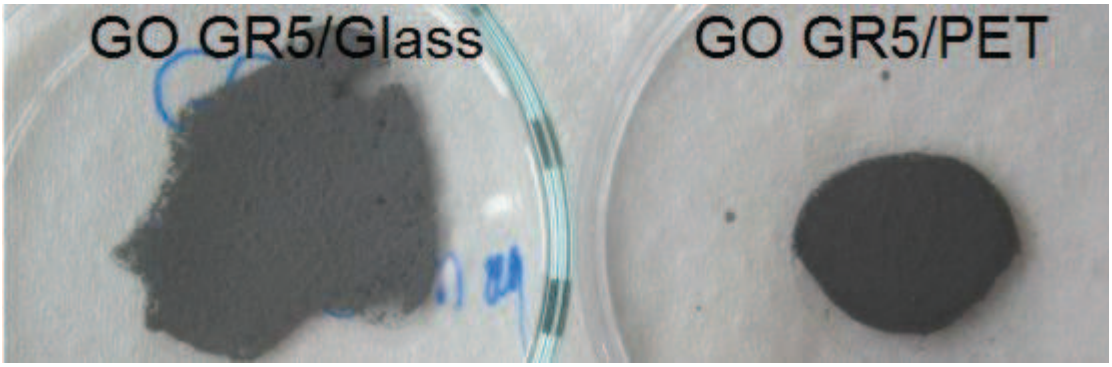

Figure 10. Thin films of GO GR5 both on glass and on PET.

Figure 10 Shows GO GR5 thin film formation. On glass looks like a fine layer in the material edges. At the same time on PET a fine layer is also formed at the edge. These phenomena mean that the use of less GO concentrated suspension can help to produce a thin film. Figure 11, shows in more details an area with thin film of GO.

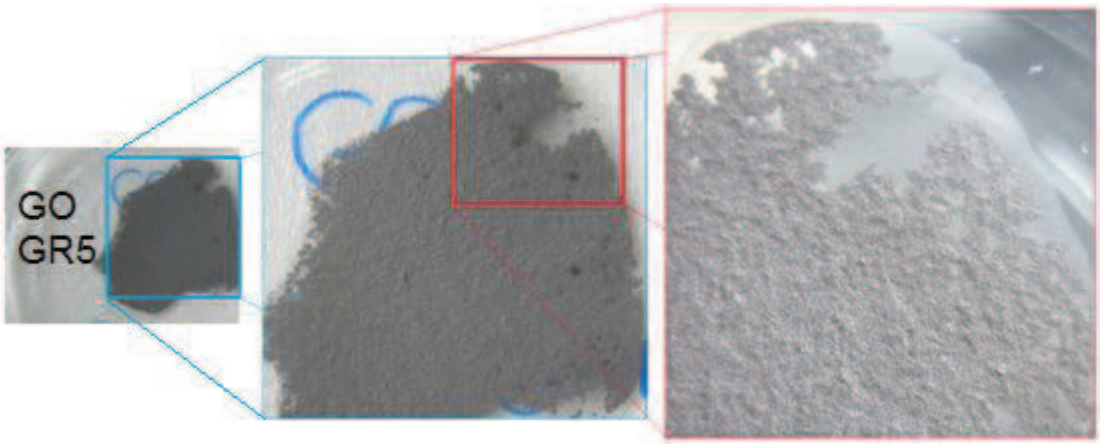

Figure11. GO GR5 thin film.

6.1.4. Reduction of GO (RGO)

Once obtained the GO suspensions, the reduction process is carried out by adding 1 μL of hydrazine hydrate for each 3 mg of corresponding GO. The mixture is keeping under stirring at 90 ºC for 2 h. Ammonia is required to ensure basic media (pH = 10.4) before hydrazine addition. GO suspensions are now electrostatic stabilized due to dissociation of carboxyl groups from GO in basic media [77 – 79].

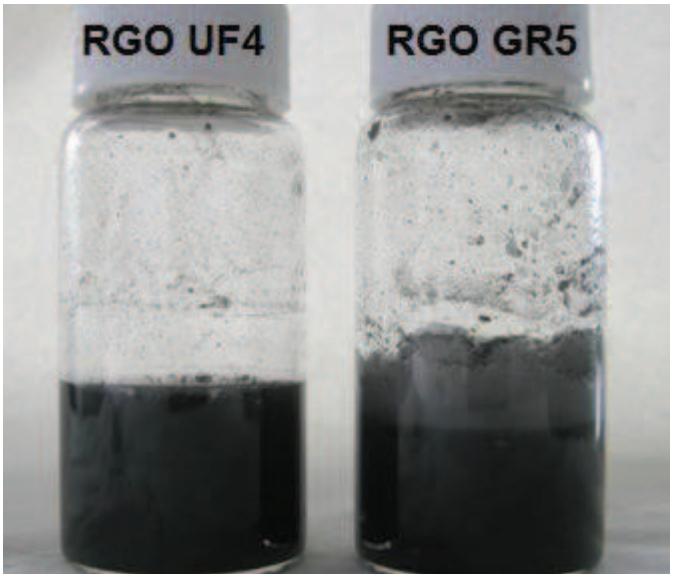

Figure 12. Reduced graphene oxide (RGO) suspensions; RGO UF4 and RGO GR5

6.1.5. RGO thin films

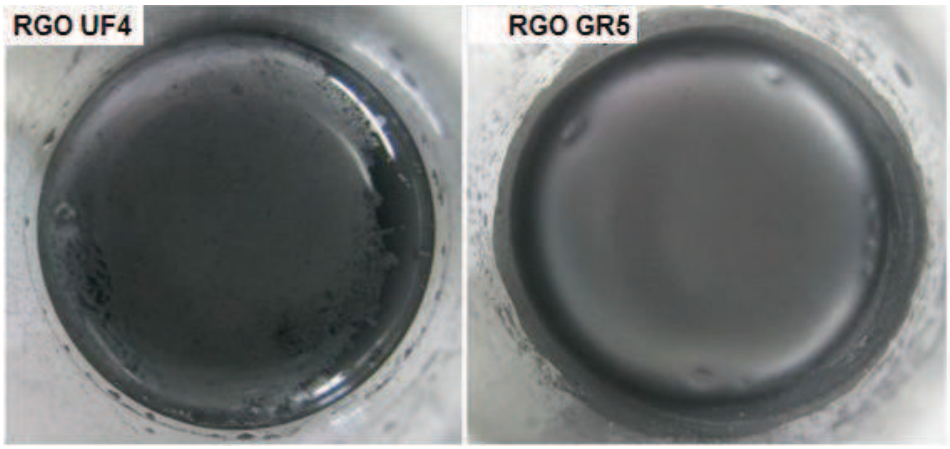

Figure 13. Top view of RGO suspensions.

Figure 13, shows the appearance of RGO suspensions. RGO UF4 has a fine layer on top of the surface and RGO GR5 looks like metallic coating highly homogeneous. Figure 14, shows a homogeneous thin film of RGO UF4 on glass substrate, while on PET substrate gave rise to an irregular distribution with evident particle agglomeration.

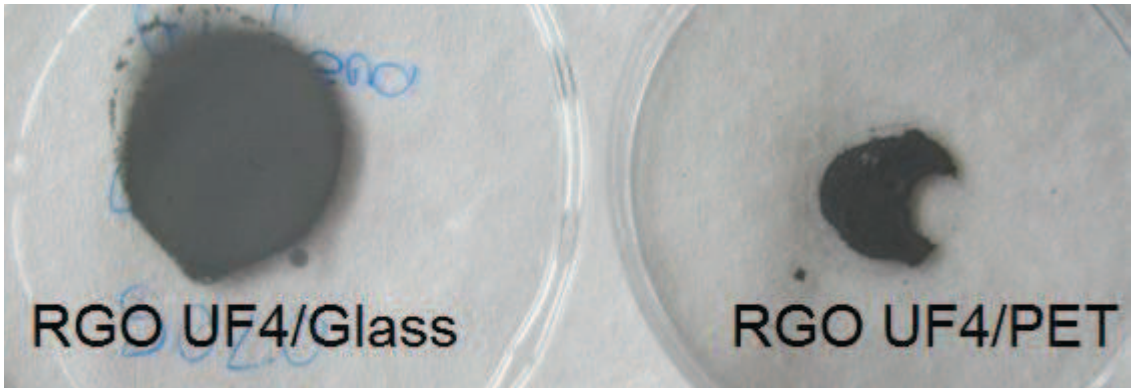

Figure 14. Thin films of RGO UF4 on glass and PET

Figure 15, shows RGO GR5 thin films. Again, glass substrate compared with PET substrate produced a more homogeneous and consistent distribution of the dispersed material.

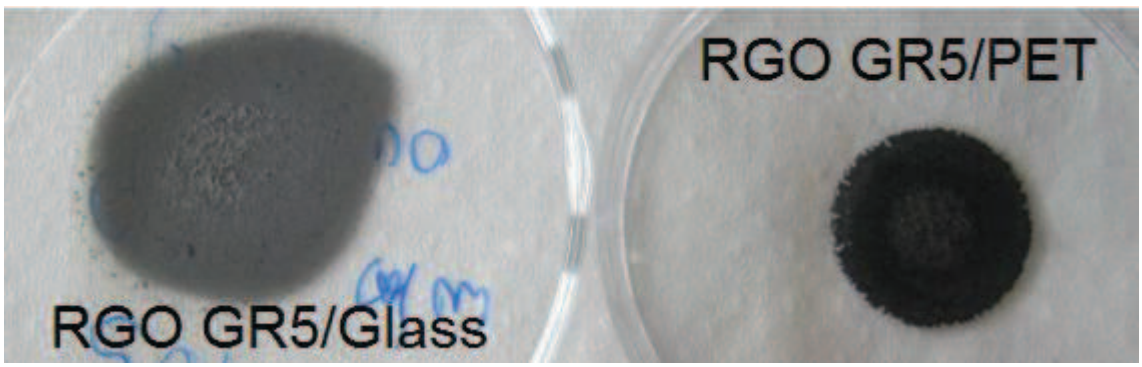

Figure 15 .Thin films of RGO GR5 on glass and PET

7. Results and analysis

7.1. Sheet resistance

The indirect measurements of the sheet resistance give us an idea about if our material is surface conductive or not. Figure 16 shows the values of sheet resistance for GO GR5 and GO UF4 on PET and glass substrates. It can be observed that the resistance value is 6 times higher when GO is dispersed on glass than on PET. Knowing that the conductivity is inversely proportional to the resistance, it is expected a higher conductivity on polymer substrate, almost by one magnitude order. These results are very interesting in the design of flexible electronic devices.

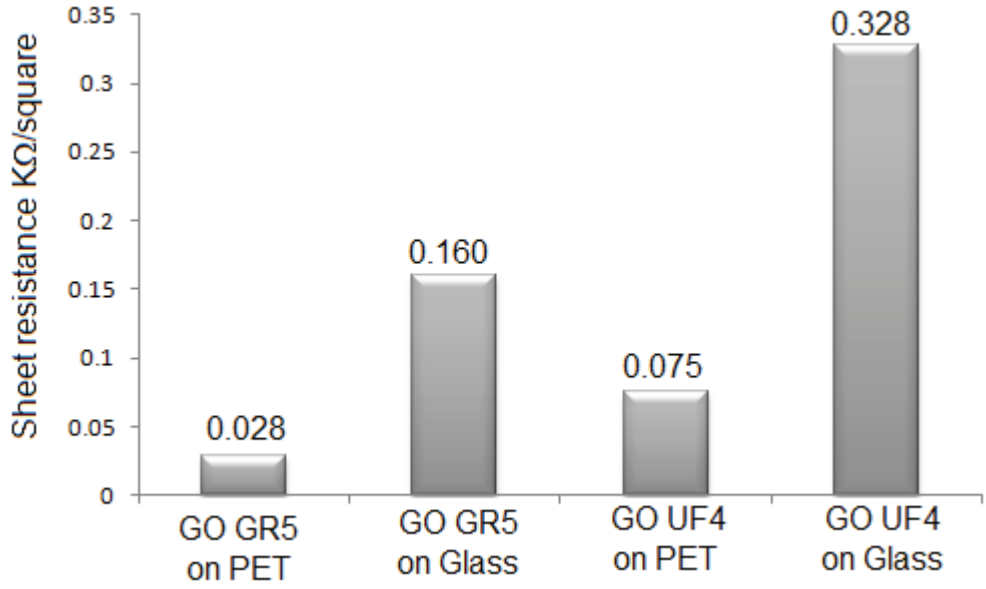

Figure 16. Sheet resistances on glass and PET, samples GO UF4 and GO GR5. Measurement deviation is less than 5%.

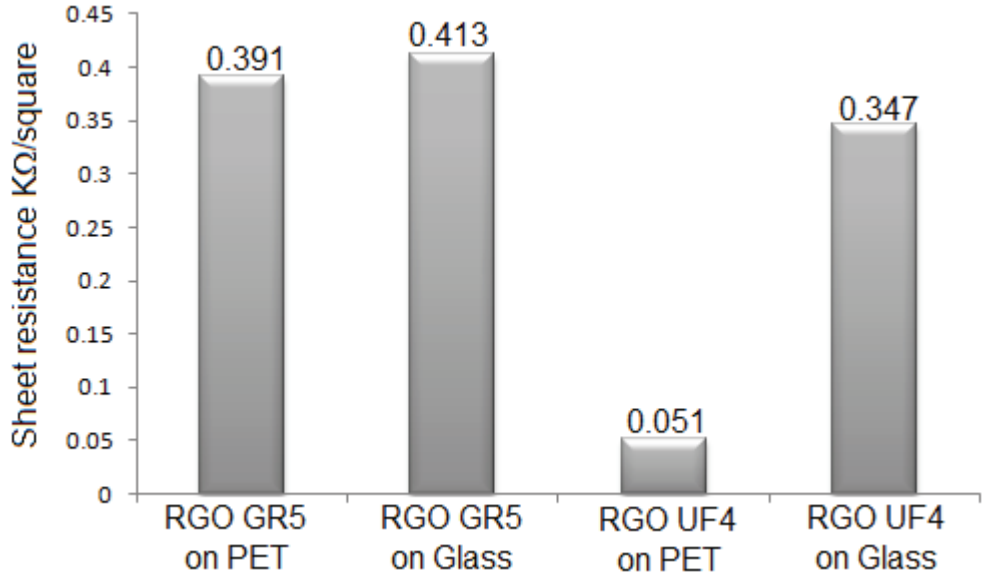

Figure 17. Sheet resistances on glass and PET, samples RGO UF4 and RGO GR5. Measurements deviation is less than 5%.

A complete characterization of the materials is required because graphene in zig-zag configuration shows conduction bands typically of the metals, while graphene chair configuration has a typical band gap of a semiconducting material [1, 7, 32].

In this case, GO GR5 sheet resistance results suggest metal bands type, while RGO GR5 behaviors as semiconducting bands. In addition, both GO UF4 and RGO UF4 samples have similar sheet resistance values, which means that GO after reduction process cannot modify significantly its bands.

7.2. SEM images

SEM images of GO UF4 with magnification of 10K and 20K show the expected stacks of laminar material (figure 18).

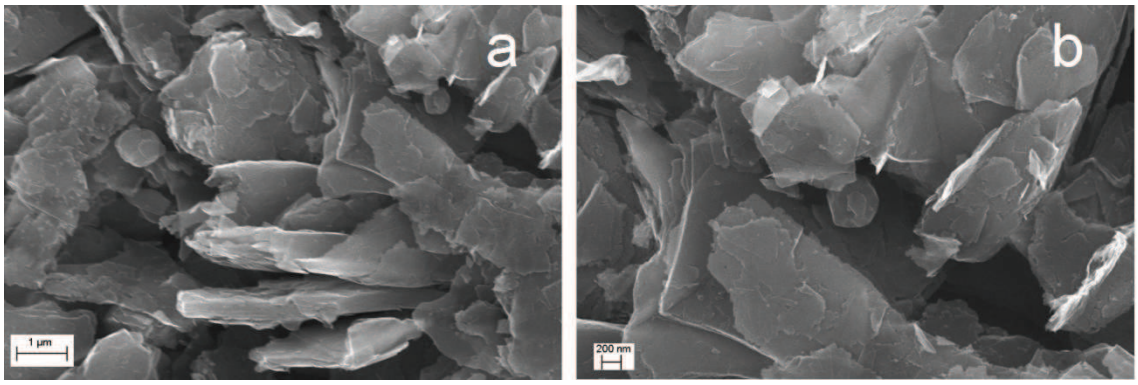

Figure 18. SEM images for GO UF4 at different magnification: a) 10K and b) 20K

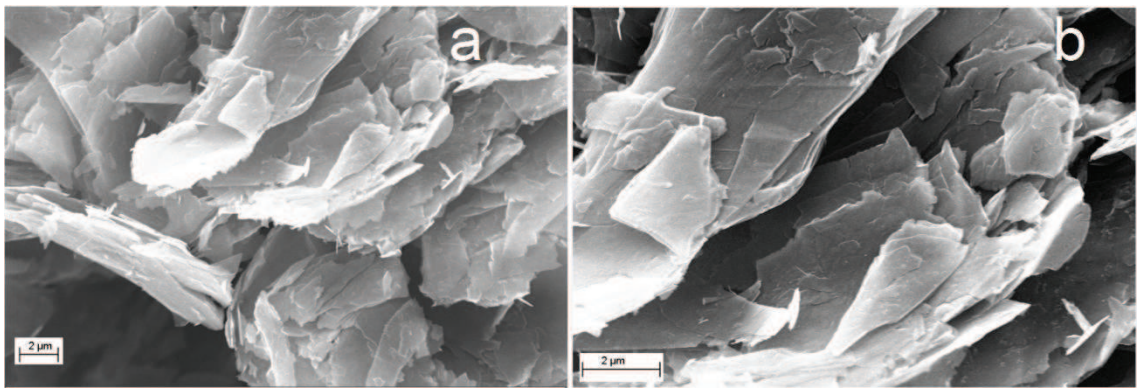

Figure 19. SEM images for GO GR5 at different magnification: a) 4K and b) 8K

GO GR5 samples exhibit finer particles (figure 19) than GO UF4. As will be shown below by TEM, this material is highly crystalline.

Regarding RGO material, RGO UF4 sample has roughness areas, multilayer zones and individual RGO layers (Figure 20), while RGO GR5 (figure 21) suggests a more efficient reduction process.

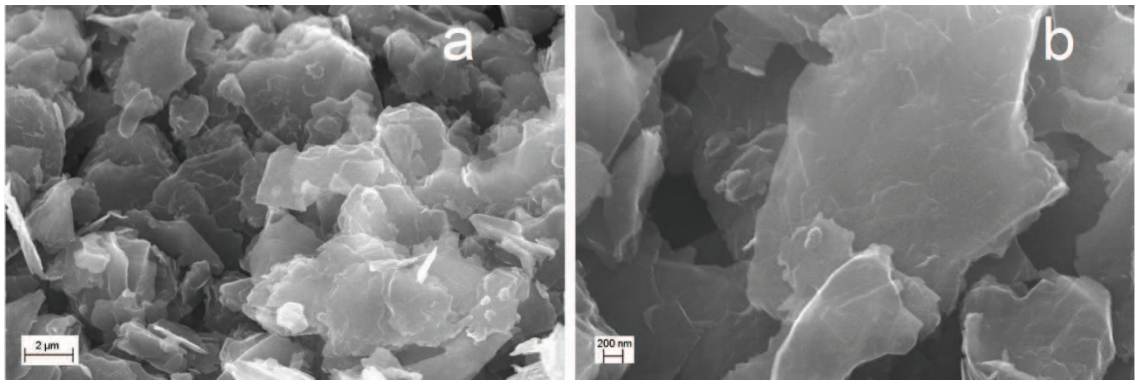

Figure 20. SEM images for RGO UF4 at different magnification: a) 5K and b) 20K

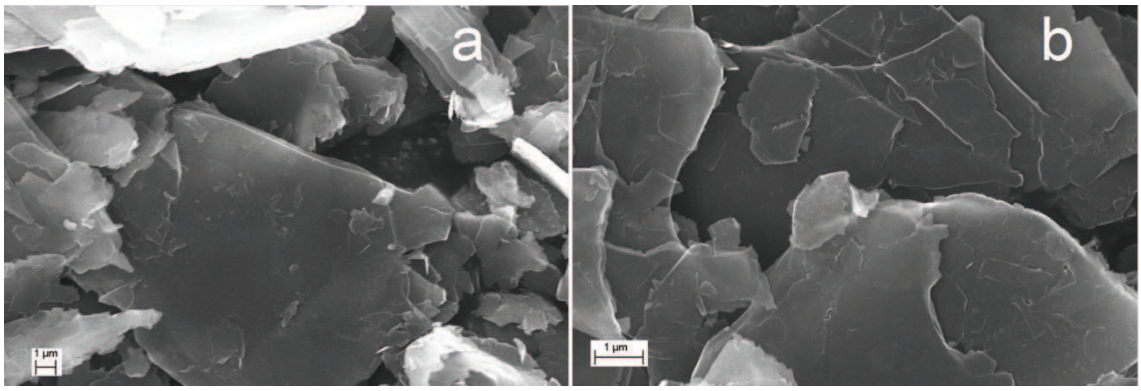

Figura 21. SEM images for RGO GR5 at different magnification a) 4K and b) 10K

7.3. TEM images

Figure 22a shows the diffraction electron pattern for GO GR5 sample. Rings with 6 equidistance bright points describing a hexagonal structure are clearly observed. The attenuated bright points may be related to an external oxidized structure. Large area particles composed of superimposed single layer of GO are evidenced in GO GR5 sample (figure 22b-d).

The electron diffraction pattern for GO UF4 samples is shown in Figure 23a. This has several bright points without equidistance gap, or perhaps such gas is not clearly distinguished. The innermost ring has a clear evidence of hexagonal type pattern. This important result allows us to deduce that despite of the use of the same oxidation process the size of the starting graphite particle plays a important role.

In fact, it can be inferred from the above results that the formation mechanism of a high ordered graphene based structure depends on the average size distribution of each precursor sample, being more favorable for smaller particles. Finally, as deduced from the comparison of Figures 22 and 23, despite of be larger size of particles in carbon UF4, after the oxidation process carried out in the same conditions GO UF4 particles are larger than those corresponding to GO GR5.

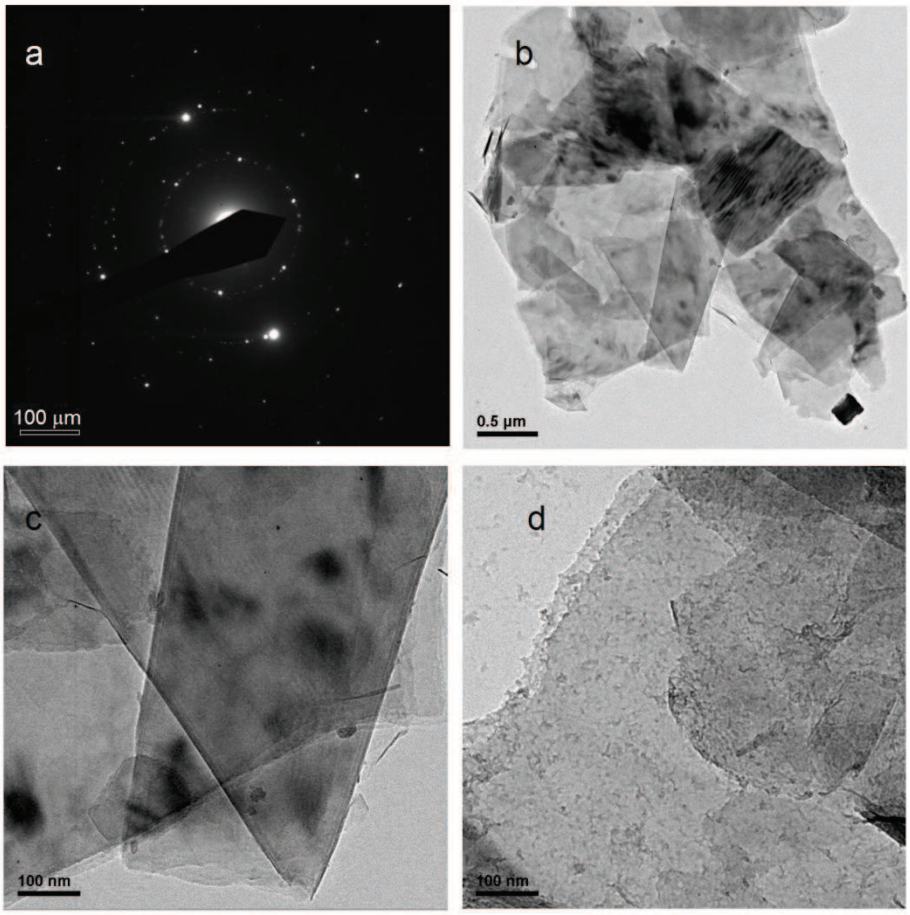

Figure 22. TEM characterization for GO GR5: a) selected area electron diffraction pattern (SAED), b) at 5K Magnification, c,d) images at 25K magnification

Figure 24 a) shows the electron diffraction pattern for RGO GR5 characterized by several bright points corresponding to areas with multilayer of graphene. TEM images of RGO GR5 taken at 25K (Figure 24b) and 60K (Figure 24d) magnifications show graphene with 1, 2 and 3 stacking layers. When the electron diffraction pattern is carried out on a single layer a hexagonal pattern is easy to identify (Figure 24c).

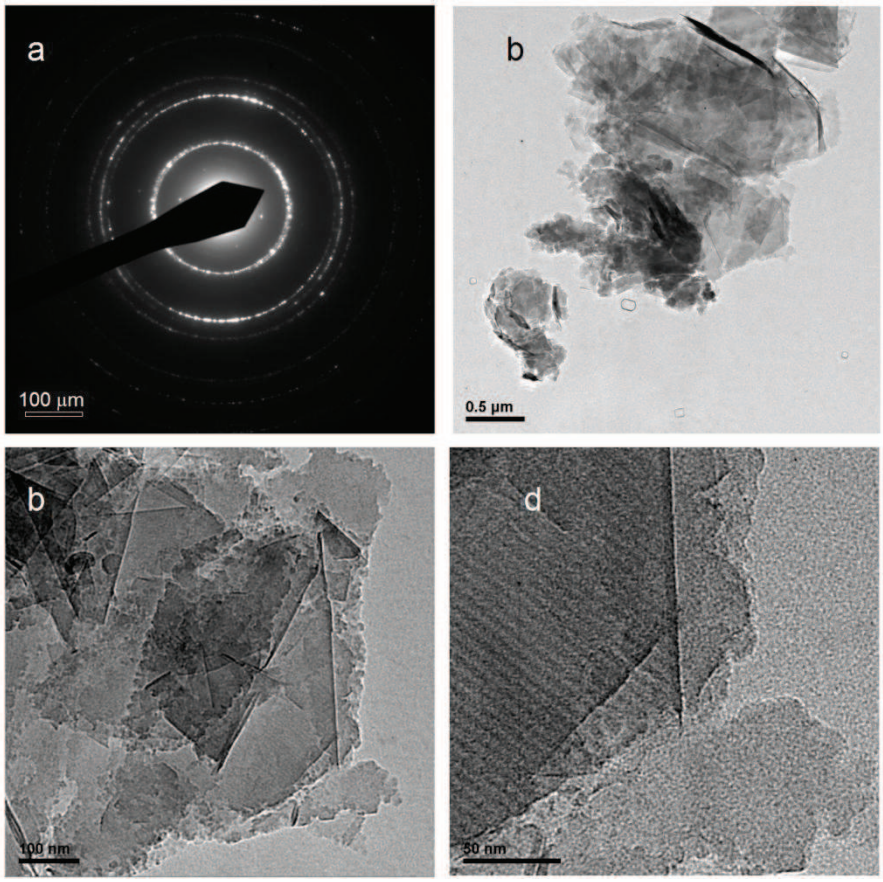

Figure 23. TEM characterization for GO UF4: a) selected area electron diffraction pattern (SAED), b) image at 5K Magnification, c) image at 25K Magnification and d) image at 80K Magnification.

RGO GR5 samples do not show an electron diffraction pattern well defined when the analysis is taken in an area of multiple layers being a polycrystalline zone, if it is compared with its respective oxide form (RGO GR5). However, when the electron diffraction analysis is carried out on a single layer, there are well defined bright points typically corresponding to a hexagonal structure (Figure 24c)

As explained above, results of RGO UF4 are different with respect to RGO GR5. The electron diffraction pattern of RGO UF4 has several bright points but the information is not enough to conclude one hexagonal structure (Figure 25a). This polycrystalline pattern could be due to staking of graphene layers in different directions.

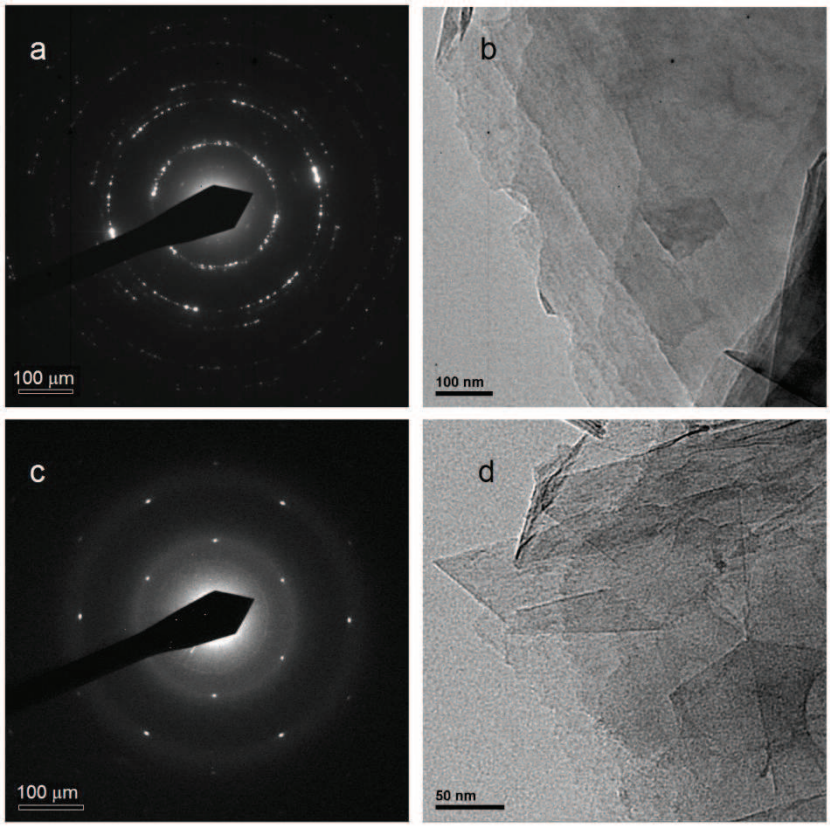

Figure 24. TEM characterization for RGO GR5: a) selected area electron diffraction pattern (SAED) on multilayer zone, b) image at 25K Magnification, c) SAED on monolayer zone, d) image at 60K magnification.

TEM images with different magnifications are also viewed where; despite to have areas characterized by multilayer aggregation the sample has areas with single graphene sheets (Figure 25c,d). The first bright ring has 6 differentiable points corresponding to [100] reflection plane and second bright ring also has 6 points corresponding to [110] reflection plane. These two signals are clues for hexagonal and single layer graphene structure.

The conclusion of the TEM analysis is that the oxidative exfoliation process is better with GR5 type graphite than with those corresponding UF4 type material. Consequently, GO and RGO GR5 would be more adequate to produce thin films of graphene or nanographite materials.

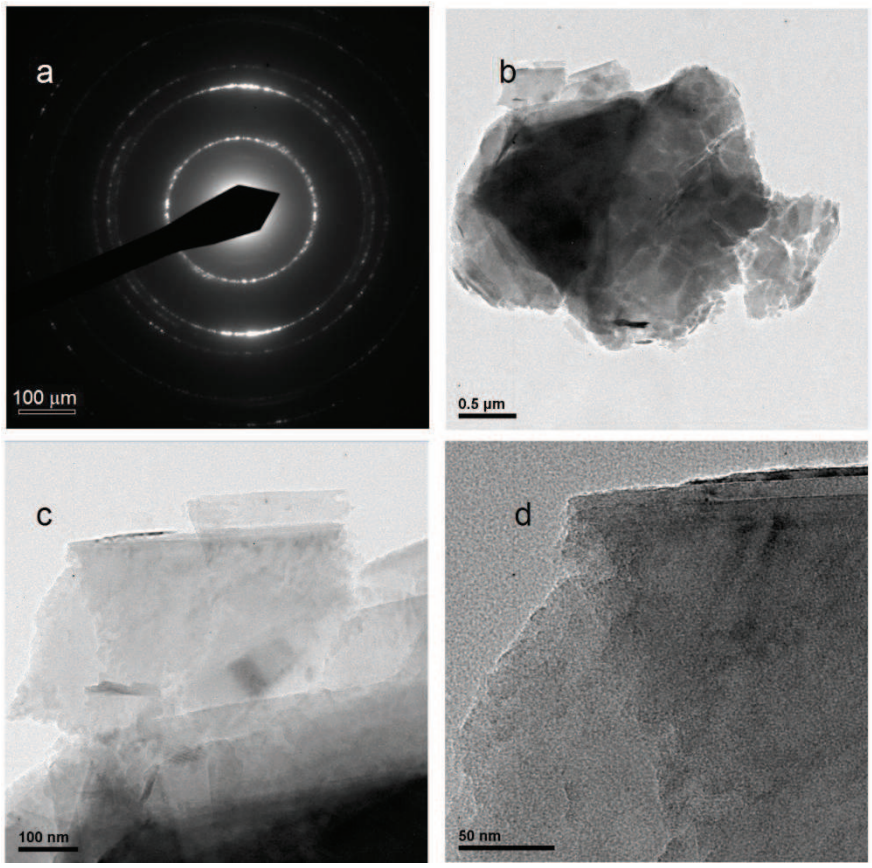

Figure 25. TEM characterization for RGO UF4 a) selected area electron diffraction pattern (SAED), b) image at 5K Magnification, c) image at 25K Magnification and d) image at 80K magnification.

7.4. FTIR analysis

According to T, Rattanaa, et al [80], the greater absorption in FTIR GO spectra correspond to oxygenated groups with a wide band in 3340 cm^{-1}, due to stretching vibration of hydroxyl O-H groups. Besides, two absorption peaks in 1730 cm^{-1} and 1630 cm^{-1} can be assigned to stretching vibrational mode of carboxylic C=O groups or carbonyl moieties. Also, two peaks near to 1226 cm^{-1} and 1044 cm^{-1}, are due to stretching vibrational mode C-O.

Figure 26 shows the FTIR spectra for synthesized GO GR5, GO UF4, RGO GR5 and RGO UF4. According to Haiqing, et al [81], the FTIR signals at 1732 and 1065 cm^{-1} are characteristic for graphene oxides, being assigned to stretching vibrational modes for C=O and C-O-C functional groups.

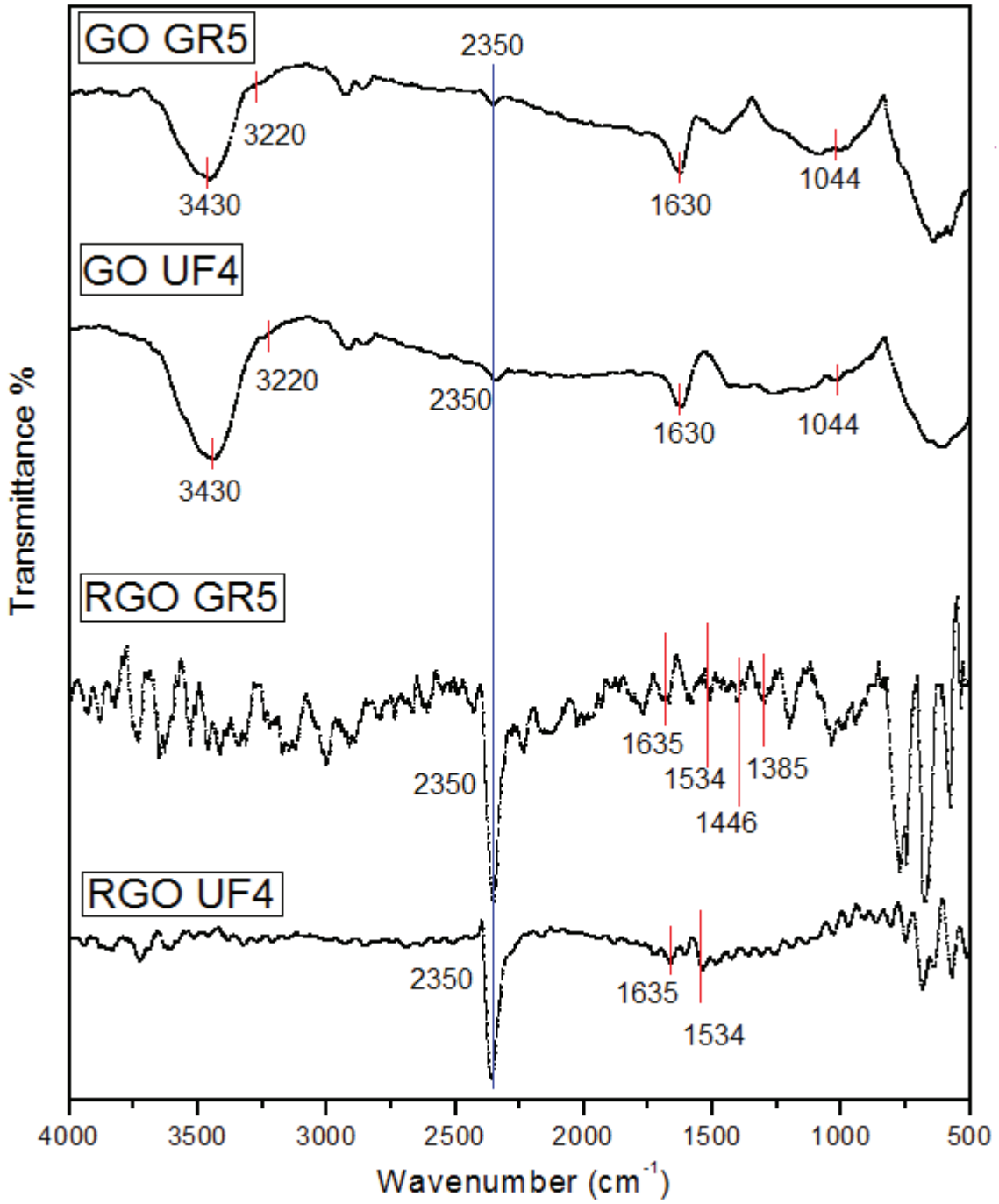

Figure. 26. FTIR spectra for GO GR5, GO UF4, RGO GR5 and RGO UF4

These signals are certainly indicating that the reduction process was effectively carried out. After Hydrazine reduction process is seen a complete disappearance of oxygenated vibrational modes is observed and a typical spectrum for graphene is evident with vibrational modes characteristics at 1385, 1446 and 1635 cm^{-1} (see Figure 26).

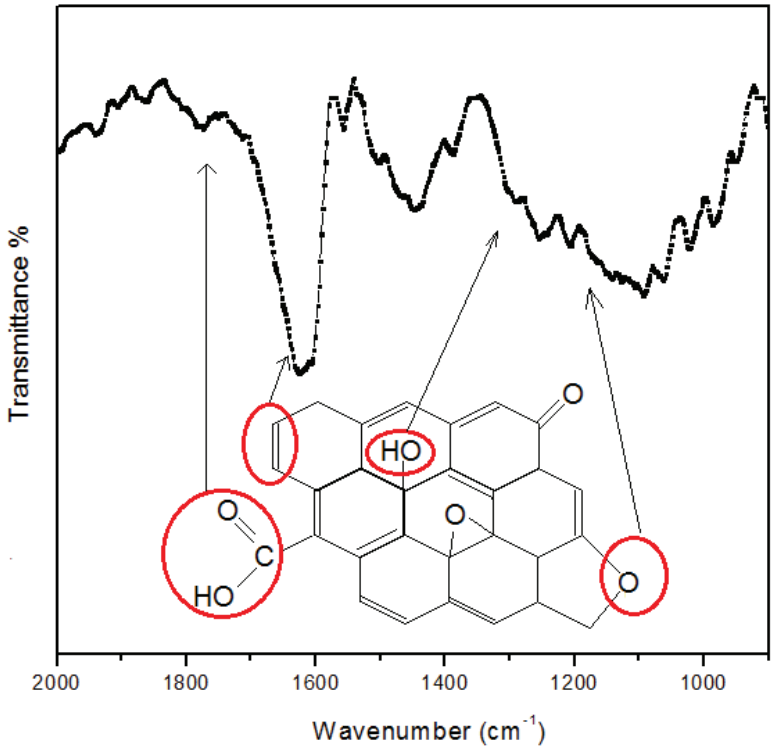

Figure 27. FTIR spectrum for GO GR5 between 2000 and 800 cm^{-1}

Figure 27 is an extension of FTIR GO GR5 spectrum, where the main functional groups and their corresponding vibrational modes are observed in detail [82].

7.5. UV absorption analysis

As above mentioned, some functional groups in both GO and RGO samples can be distinguished by FTIR; however, low resolution in some diagnostic signals does not allow a clear identification. Using UV absorption spectroscopy it was possible to identify some peaks corresponding to interest transitions.

Figure 28 show the UV absorption spectra for GO UF4 and RGO UF4 suspension samples between 200 and 340 nm. Water was used as blank. At 230 nm, it appears one shoulder due to particles or nano-sheets of GO. This corresponds to the $\pi-\pi*$ transition from an aromatic bonding system C-C type. This is seen in GO UF4 sample but not in RGO UF4.

Further near to 250 and 325 nm, it appears a wide shoulder shifted to left side indicating $\pi-\pi*$ transition due to carbon oxygen C=O bonds [80]. The absence of these two signals in OGR UF4 sample indicates that the material is totally reduced or that the amount of remanent oxygenated moieties is low.

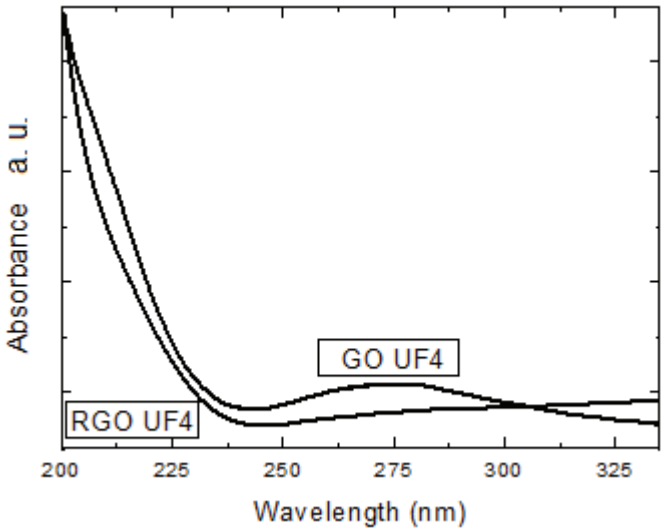

Figure 28.UV Absorption spectra for GO UF4 and RGO UF4.

Figure 29 shows the UV absorption spectra for GO GR5 and RGO GR5. The mentioned shoulder at 230 nm is clearly seen; this corresponds to $\pi-\pi*$ transition of aromatic system based on C-C type bond. Two shoulders between 250 and 325 nm correspond to $\pi-\pi*$ transition of carbon oxygen C=O type bond. UV spectrum for RGO GR5 does not show the peaks for oxygenated moieties transitions. This suggests that the reduction process was carried out successfully. The almost totally absence of 230 nm signal corresponding to aromatic system means that some areas of the sample are remaining as C=C type bonds, typically for a graphene structure.

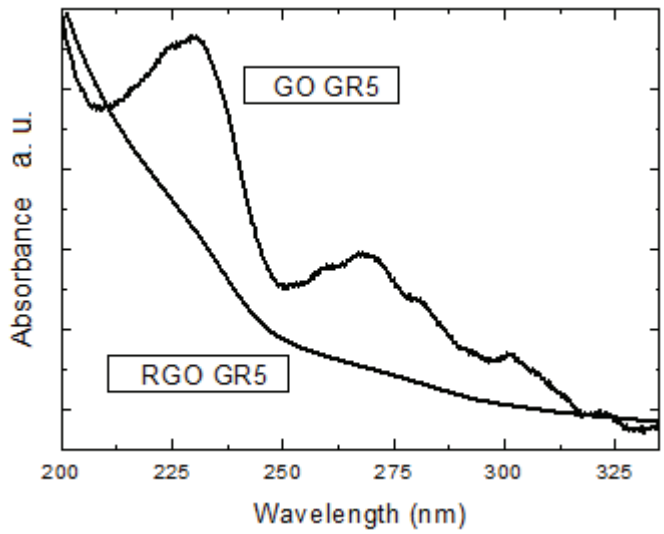

Figure 29. UV absorption spectra for GO GR5 and RGO GR5

7.6. TGA analysis.

The thermogravimetric analysis of samples GO UF4, GO GR5, RGO UF4 and RGO GR5 were carried out in air atmosphere is shown in Figure 30. The mass losses were already measurable at 100 ºC for GO type samples due to their hydrophilic nature which allowed water retention.

Both GO UF4 and RGO UF4 show different thermal decomposition behavior compared with GO GR5 and RGO GR5. However, GO GR5 is thermally unstable and starts to lose mass upon heating even below 100 ºC, the early important mass loss that occurs at 200 ºC (more than 10% of starting mass), due to pyrolysis of the labile oxygen moieties, allowing CO_2, CO, and steam [83, 84].

Thermal decomposition of GO GR5 would be accompanied by gas evolution, causing a fast thermal expansion of GO. On the other hand, the removal of the thermally labile oxygen functional groups by chemical reduction results in much increased thermal stability for the RGO GR5. Besides, RGO samples became hydrophobic and no appreciable mass loss (close to 100 ºC due to water adsorption) is observed below 300 ºC [85].

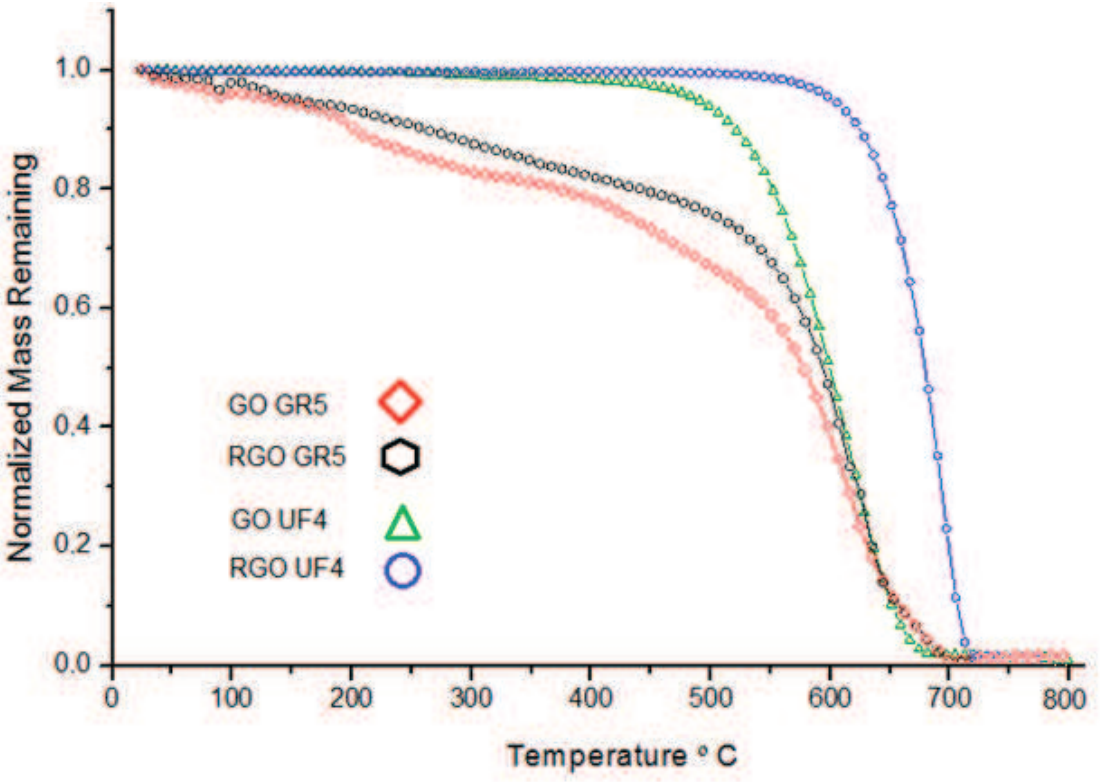

Figure 30. Normalized TGA curves for GO GR5, GO UF4, RGO GR5 and RGO UF4. For GO samples, pyrolysis of oxygenated groups to CO, CO_2 and water removal produces mass losses between 150 and 350; from about to 350 to 550 ºC remains from pyrolysis are decomposed. For both GO and RGO samples, above 550-600 ºC the carbon skeleton starts its complete degradation ºC. Scan velocity 1ºC/min in air flux.

Two significant losses are evident in GO GR5, first one between 200 ºC to 300 ºC corresponding to 20% of starting mass, and second occurs between 400 ºC to 700 ºC having a dramatically loss at 600 ºC. Meanwhile, between 200 ºC and 550 ºC there is a loss close to 20% of starting mass of RGO GR5, above 550 ºC decomposition of RGO GR5 occurs very fast, and in 750ºC decomposition mass occurs totally. In the other hand, GO UF4 and RGO UF4 have only one thermal transition of the decomposition process. In general, oxidized sheets can decompose at less temperature compare with their reduced ones.

7.7. XRD analysis

X-ray diffraction technique was used in order to know in more detail the crystallographic structure of GO GR5 and RGO GR5. GR5 type samples were selected due to their better properties compared with UF4 graphite type material as mentioned above.

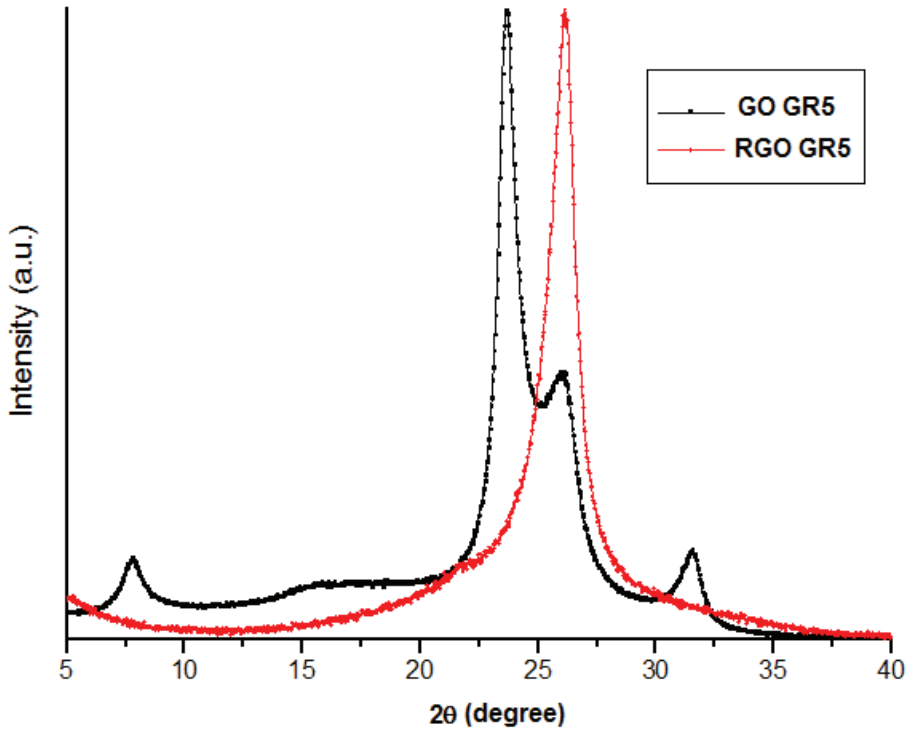

Figure 31. XRD pattern of GO GR5 and RGO GR5

The signal wide spread between 12.5º and 18.3º in 2θ degree is typical for graphene and graphite oxides (Figure 31). After hydrazine reduction this signal disappears and a high intensity signal appears between 20.0º to 30.0º in 2θ degree corresponding to graphene structure. This high intensity corresponds with the information acquired in SAED analysis showing in Figure 24c, where a graphene hexagonal monolayer is evident.

8. Grätzel cell

Dye sensitized solar cells (DSSC) are unique compared with almost all other kinds of solar cells in that electron transport, light absorption and hole transport are each handled by different materials in the cell [86, 87]. The sensitizing dye in a DSSC is anchored to a wide-band gap semiconductor such as TiO_2, SnO_2 or ZnO. When the dye absorbs light, the photoexcited electron rapidly transfers to the conduction band of the semiconductor, which carries the electron to one of the electrodes [88]. A redox couple, usually comprised of iodide/triiodide (I^- /I_3^-), then reduces the oxidized dye back to its neutral state and transports the positive charge to the counter-electrode [89].

In 1991, O'Regan and Gratzel demonstrated that a film of titania (TiO_2) nanoparticles deposited on a DSSC would act as a mesoporous n-type photoanode and thereby increase the available surface area for dye attachment by a factor of more than a thousand [90]. This approach dramatically improved light absorption and brought power-conversion efficiencies into a range that allowed the DSSC to be viewed as a serious competitor to other solar cell technologies [91]. A schematic and energy level diagram showing the operation of a typical DSSC is shown in Figure 32.

During the 1990s and the early 2000s, researchers found that organometallic complexes based on ruthenium provided the highest power-conversion efficiencies [93, 94]. Iodide/triiodide was found to be the most effective redox couple [95 – 99]. The record power-conversion efficiency rapidly climbed to 10% in the late 1990s and then slowly settled to 11.5% [100 – 103].

The iodide/triiodide system has been particularly successful in DSSC because of the slow recombination kinetics between electrons in the titania with the oxidized dye and the triiodide in the electrolyte, which leads to long-lived electron lifetimes (between 1 ms and 1 s) [104 – 106]. Iodide reduces the oxidized dye to form an intermediate ionic species (such as $I\bullet_2^-$) that then disproportionates to form triiodide and diffuses to the counter-electrode, providing two electrons per molecule. The slow recombination and relatively fast dye regeneration rates of the I^-/I_3^- redox couple have resulted in near-unity internal quantum efficiencies for a large number of dyes, providing the high external quantum efficiencies. The small size of the I^-/I_3^- redox components allows for relatively fast diffusion within the mesopores, and the two-electron system allows for a greater current to be passed for a given electrolyte concentration. Unfortunately, the I^-/I_3^- system is corrosive and dissolves many of the commonly used sealants and metal interconnects (such as silver, copper, aluminium and gold).

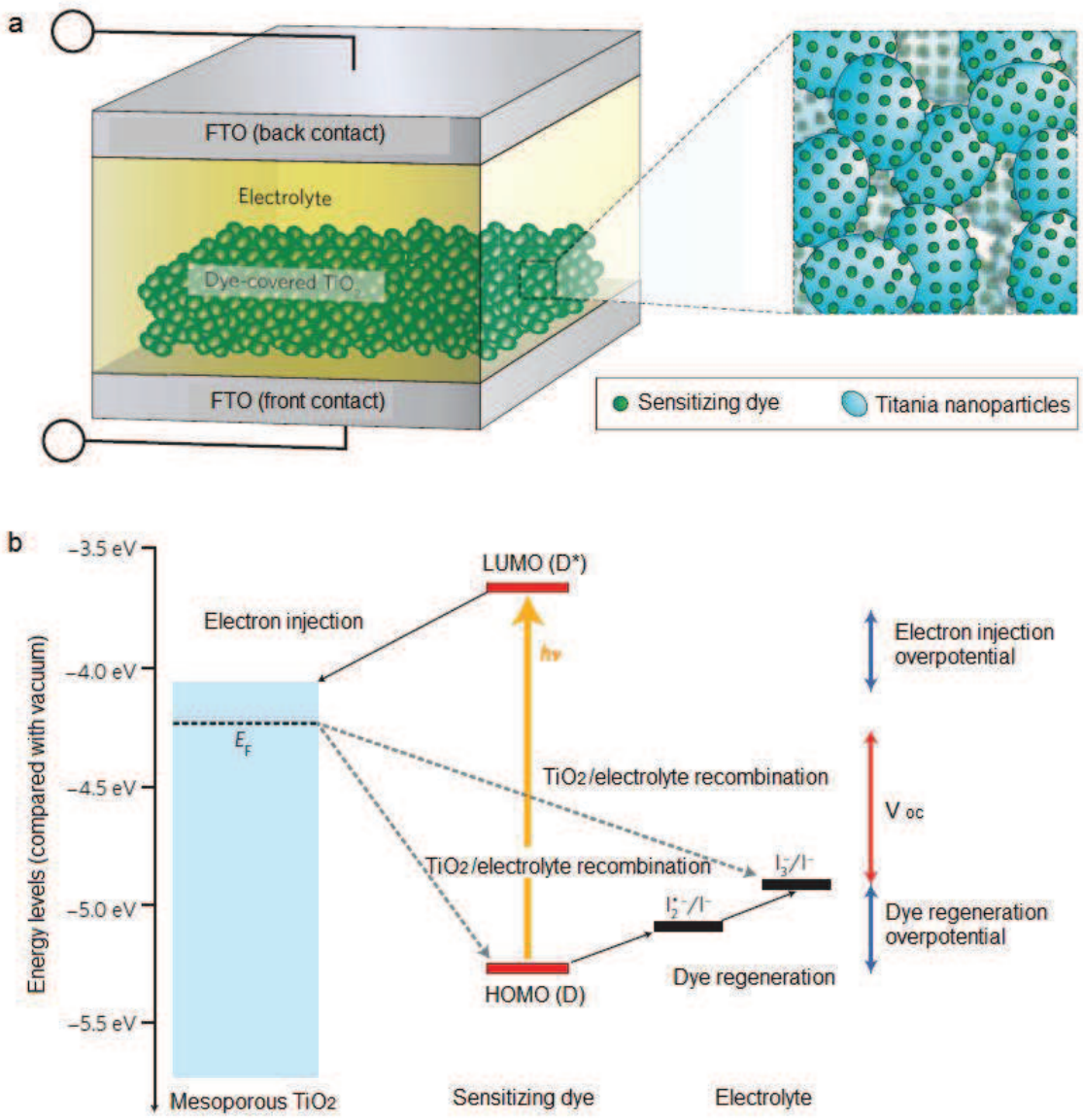

Figure 32. Dye-sensitized solar cell device schematic and operation. **a**, Liquid-based DSSC are comprised of a transparent conducting oxide (such as fluorine-doped tin oxide, FTO) on glass, a nanoparticle photoanode (such as titania) covered in a monolayer of sensitizing dye, a hole-conducting electrolyte and a platinum-coated, FTO-coated glass back-contact [92]. **b**, Energy level and device operation of DSSC; the sensitizing dye absorbs a photon (energy *hv*), the electron is injected into the conduction band of the metal oxide (titania) and travels to the front electrode. The oxidized dye is reduced by the electrolyte, which is regenerated at the counter-electrode to complete the circuit. V_{OC} is determined by the Fermi level (E_F) of titania and the redox potential (I_3^-/I^-) of the electrolyte.

8.1. DSSC building up

Soda lime glass (SLG) and PET (polyethylene terephthalate) are the substrates used for building up the sensitized dye solar cells (DSSC) devices. TiO_2 was used as semiconducting electrode. Thus, a water slurry of TiO_2 rutile was prepared and used to carry out coatings on both SLG and PET substrates. Doctor blade equipment with micrometric screw system was used to obtain homogeneous and continuous TiO_2 thin film.

Taking in to account that PET starts to melt close to 200 ºC, annealing processes can be carried out below this temperature without GO or RGO significant thermal decomposition. Thus annealing process was carried out at 50, 100, 150 y 200 ºC in an air controlled oven in order to identify optimal temperature that allows proper and mechanically attach of TiO_2 on PET and glass substrates. However, at more than 150 ºC TiO_2 cannot be attached to the PET surface, and the chosen temperature that allows the attachment of TiO_2 on PET substrate with high adherence was 100 ºC.

The selected dye was tris(2,2´bipyridyl dichlororuthenium (II)) hexahydrate (TBDR) [93, 94]. TBDR (0.0115 g) was solved in ethanol (5 mL). Iodine crystals (0.127 g) and potassium iodide (0.130 g) were dispersed in ethylene glycol (10 mL) in order to produce the liquid media pair redox (I_3^-/I^-). All above mentioned reactants were obtained from Sigma–Aldrich and were of high purity. Figure 31 shows the scheme of built Gätzel cells both using PET and SLG substrates.

Photovoltaic solar cell analyzer ISM 490 ISO-TECH was used to determine the photovoltaic parameter in the built solar cell devices, with resolution tension of 0.001 V, and resolution current of 0.001 mA. Halogen lamp was used to illuminate the cell with a separation distance of 10 cm, in standard illumination conditions: irradiance 1000 W/m^2, spectral distribution AM 1.5 and normal incidence. A commercial CIGSe cell of $CuIn(S,Se)_2$ was used to determine the photovoltaic parameters. Taking in to account that these measurements were not carried out in the conventional solar simulator where the electric contact tips are enough sensitive to detect low electrical currents, then the photovoltaic parameters of CIGSSe cell were used. In order to analyze how these parameters decrease when the cell is connected in a series circuit to a lab-made Grätzel cell device. This CIGSe cell under above mentioned standard illumination conditions has V_{oc} 6.593 V, J_{sc} 4.9 mA cm^{-2}, fill factor (0.77 %) and efficiency η of 17.7%. See annexes 1 in order to understand PV calculations.

8.2. PV parameters analysis

Table 3 show the PV parameter V_{oc}, J_{sc} and η efficiency for TDBR cover concentration as mentioned in figure 32. The GO and RGO suspensions used for these cells was GR5 because the graphite precursor showed better results as described in above mentioned analyses.

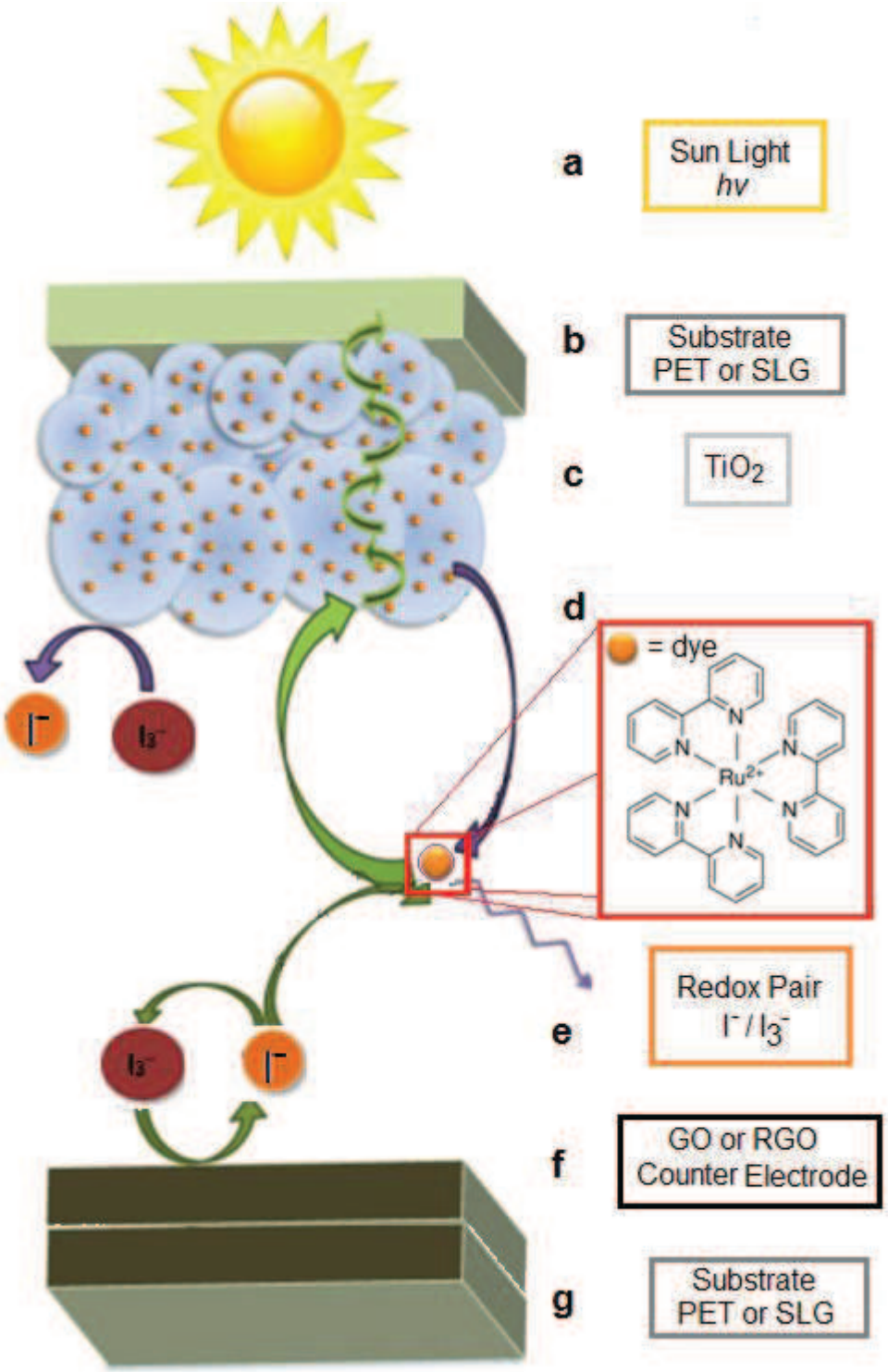

Figure 32. Scheme of Grätzel photovoltaic solar cell device: a) sun light with enough energy that allows electronic transfer between dye/TiO_2 surfaces and external electric circuit; b) transparent substrate in this case glass or PET; c) titanium dioxide thin film coated by Doctor blade technique (0.05 mm thickness); d) few drops of TBDR ethanol solution is added to TiO_2 surface (enough to cover all area); e) iodine crystals and potassium iodide are mixed in ethylene glycol in order to produce the liquid media pair redox (I_3^-/I^-); f) GO or RGO suspensions were coated by Doctor blade technique on g) PET or SLG substrates. Transparent Scotch tape is used to seal all devices.

Type of cell	V_{oc} (mV) per 1cm^2	J_{sc} (mA cm^{-2}) x 10^{-2}	η %
SLG/TiO_2/TBDR/(I_2/I^-_3)/RGO/SLG	41.2 ± 3.6	3.1 + 0.3	0.11
PET/TiO_2/TBDR/(I_2/I^-_3)/RGO/PET	70.4 ± 5.6	5.2 + 0.4	0.19
SLG/TiO_2/TBDR/(I_2/I^-_3)/GO/SLG	56.8 ± 3.2	4.2 + 0.2	0.15
PET/TiO_2/TBDR/(I_2/I^-_3)/GO/PET	94.4 ± 5.6	7.0 + 0.4	0.25

Table 3. PV parameters for different Gätzel solar cell devices with TBDR cover concentration GO and RGO correspond to GR5 type material.

Type of cell	V_{oc} (mV) per 1cm^2	J_{sc} (mA cm^{-2}) x 10^{-2}	η %
SLG/TiO_2/TBDR/(I_2/I^-_3)/RGO/SLG	52.0 ± 2.2	3.9 + 0.2	0.14
PET/TiO_2/TBDR/(I_2/I^-_3)/RGO/PET	76.9 ± 3.1	5.7 + 0.2	0.20
SLG/TiO_2/TBDR/(I_2/I^-_3)/GO/SLG	38.0 ± 2.2	2.8 + 0.2	0.10
PET/TiO_2/TBDR/(I_2/I^-_3)/GO/PET	36.0 ± 1.4	2.7 + 0.1	0.09

Table 4. PV parameters for different Gätzel solar cell devices with TBDR three times cover concentration GO and RGO correspond to GR5 type material.

With the next equation is possible to calculate the decreasing value of the CIGSSe cell efficiency due to the in series connection with Grätzel cell:

$$\mathbf{A_T} * \mathbf{n_T} = (\mathbf{A_1} * \mathbf{n_1}) + (\mathbf{A_2} * \mathbf{n_2})$$

where A_T is the total area (area of CIGSSe cell and Grätzel cell exposed to standard lighting), n_T is the efficiency reported by the equipment after the standard illumination process, A_1 is the area of CIGSSe cell, A_2 is the area of Grätzel cell, n_1 is the CIGSSe efficiency which is 17.7% as mentioned before and n_2 is the unknown variable.

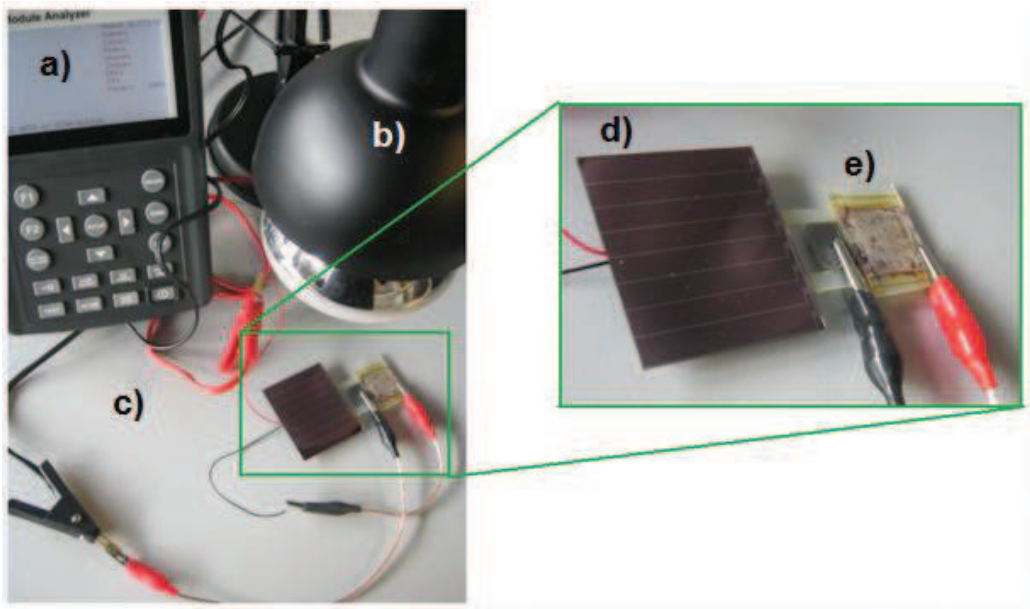

Figure 31. Scheme of I-V curve measurement: a) acquisition data equipment, b) halogen lamp, c) electrical connections, d) CIGSSe solar cell device and e) Grätzel lab made solar cell device.

Figure 31 show the scheme of the equipment used for taking of the PV parameters. Once the lamp is turn on, 1 min is waited before to start the measurements, the acquisition data information is achieved after 20 or 30 seconds. The caiman connections must to be well connected and verify the serials configuration before to start with the illumination process.

Comparing the results showing in tables 3 and 4, V_{oc} is higher in PET flexible device compared with SLG devices. Besides, better results are achieved when PET is used as substrate and when the GO GR5 is used as counter electrode and TBDR cover concentration is coated one time. However, when the TBDR concentration is coated three times both cells that have RGO show an increment of 26% in the V_{oc} for SLG device and an increment of 9.2% for PET device, meanwhile GO devices have a reduction of 33% for PET and 61% for SLG. Then, the highest efficiency η is achieved by PET/TiO_2/TBDR/(I_2/I^-_3)/GO/PET device with 0.25% (one TBDR coating) and by PET/TiO_2/TBDR/(I_2/I^-_3)/RGO/PET device with 0.20% (three TDBR coating).

9. Conclusions

- Starting with small graphite particles is better compared with great ones. SEM images allow distinguishing, that despite GR5 particles are smaller than UF4 particles the resulting GO and RGO materials for GR5 particles are bigger than GO UF4 and RGO UF4, forming laminar materials with hundreds of nanometers in area (0.5 μm x 1.0 μm).

- Resulting suspensions of GO and RGO were highly stable in water avoiding the settling process. Those suspensions are potential inks for coming solar flexible device generation based on printable materials.

- TEM characterization shows that GO and RGO (both from GR5 material) have particles in monolayer form by hundreds of nanometers in area (0.5 μm x 1.0 μm). This behavior ends in highly electrical properties for samples GR5 compared with UF4. XRD analysis also corroborates that GO GR5 after hydrazine reduction process allows obtaining highly oriented and delaminated graphene-sheets. However, there are material zones where particles have several carbon layers, being a material not homogeneous. This suggests, that wet method is less efficient compared with PVD (physical vapor deposition) and CVD (chemical bath deposition) processes.

- Oxidative exfoliation Hummers process is reproducible in order to obtain GO, and after hydrazine RGO can be obtained, as corroborated both by UV absorption and FTIR spectra. However, the final electrical properties depend on the starting particle size. Large particles have low electrical properties, while small particles have good electrical properties; this is related with their capability of forming thin films. The GO sheet resistance is 0.028 kΩ/square on PET, compared with 0.160 kΩ/square on glass, being this material the most appropriate to be used as counter

electrode in DSSC devices, if it is compared with the RGO which is 0.391 kΩ/square on PET and 0.413 KΩ/square on glass.

- In the built Grätzel solar cell devices the highest efficiency is achieved by PET/TiO_2/TBDR/(I_2/I^-_3)/GO/PET configuration with 0.25% (one TBDR coating) and by PET/TiO_2/TBDR/(I_2/I^-_3)/RGO/PET configuration with 0.20% (three TDBR coating).

- The possibilities and becoming applications of GO and RGO materials are not limited only to the photovoltaic area; other several applications like in fuel cell, catalysis processes, composites, membranes and thermoelectric materials can be achieved taking into account the results of this final master thesis work.

10. Acknowledgment

To Universidad de Zaragoza specially to INA (Instituto de Nanociencia de Aragón), GREG group led by Dr. Joaquín Coronas y Carlos Téllez. To PhD student Sonia Castarlenas for her patience and unconditional collaboration, and all other technical, students and staff of GREG group. To Semiconducting Materials and Solar Energy Lab from Universidad Nacional de Colombia led by Gerardo Gordillo for use some specific substrates ITO based and IREC Barcelona for SEM service in the Functional Nanomaterial Group led by Andreu Cabot. And also, to Pilar Cea Director of Nanomat Master programme and Fundación Carolina scholarship.

11. References

[1] J.W. Martin. Concise Encyclopedia of the structure of materials. Editor University of Oxford, UK. 2007 Elsevier Ltd. Page 60 to 68.
[2] H-S. Philip Wong., Deji, Akinwande. Carbon Nanotubes and Graphene Devices. Cambridge University Press 2011. First Edition, ISBN 978-0-521-51905-2.
[3] Jonathan W. Steed., Jerry L. Atwood. Supramolecular chemistry, Second Edition. 2009 John Wiley & Sons, Ltd ISBN: 978-0-470-51233-3. Pag 935
[4] K.S. Novoselov et al., Nature 438, 197 (2005)
[5] Y.B. Zhang et al., Nature 438, 201 (2005)
[6] K.S. Novoselov et al., Science 306, 666 (2004); Proc. Natl. Acad. Sci. USA 102, 10451 (2005)
[7] M.I. Katsnelson, Materials Today 10, Jan–Feb 2007, p. 20
[8] Y. Zhang et al., Nature 438, 201 (2005)
[9] A.C. Ferrari et al., Phys. Rev. Lett. 97, 187401 (2006)
[10] R.E. Peierls, Ann. I. H. Poincaré 5, 177 (1935)
[11] L.D. Landau, Phys. Z. Sowjetunion 11, 26 (1937)
[12] N.D. Mermin, Phys. Rev. 176, 250 (1968)
[13] D.R. Nelson et al., eds., Statistical Mechanics of Membranes and Surfaces (World Scientific, Singapore, 2004)
[14] J.C. Meyer et al., Nature 446, 60 (2007)
[15] X. Jia et al., Science 323, 1701 (2009)
[16] M. Terrones, Nature 458, 845 (2009
[17] P.R. Wallace, Phys. Rev. 71, 622 (1947)
[18] A.K. Geim, K.S. Novoselov, Nat. Mater. 6, 183 (2007)
[19] A.H. Castro Neto et al., Rev. Mod. Phys. 81, 109 (2009)
[20] K.L. Wang et al., Proc. IEE. 96, 212 (2008)
[21] M. Choucair et al., Nat. Nanotechnol. 4, 30 (2009)
[22] G. Brumfiel, Nature 458, 390 (2009)
[23] R.J. Young. Composites Science and Technology. 72 (2012) 1459–1476
[24] F.D. M. Haldane, Phys. Rev. Lett. 61, 2015 (1988)
[25] E. Stolyarova et al., Proc. Natl. Acad. Sci. USA 104, 9209 (2007)
[26] M.H. Gass et al., Nat. Nanotechnol. 3, 676 (2008)
[27] J.C. Meyer et al., Nano Lett. 8, 3582 (2008)
[28] C.Ö. Girit et al., Science 323, 1705 (2009)
[29] J.W. Seo et al., Angew. Chem. Int. Ed. 46, 8828 (2007)
[30] K.S. Novoselov et al., Science 315, 1379 (2007)
[31] Z.Q. Li et al., Nat. Phys. 4, 532 (2008)
[32] W.Y. Kim, K.S. Kim, Nat. Nanotechnol. 3, 408 (2008)
[33] Y.M. Zuev et al., Phys. Rev. Lett. 102, 096807 (2009)
[34] L. Tabasztó et al., Nat. Nanotechnol. 3, 397 (2008)
[35] X.T. Jia et al., Science 323, 1701 (2009)
[36] L. Jiao et al., Nature 458, 872 (2009)
[37] Y.M. Lin et al., Nano Lett. 9, 422 (2009)
[38] J.Y. Huang et al., Phys. Rev. Lett. 98, 185501 (2007)
[39] E. McCann, V.I. Fal'ko, Phys. Rev. Lett. 96, 086805 (2006)
[40] K.S. Novoselov et al., Nat. Phys. 2, 177 (2006)
[41] J.M. Ziman, *Models of Disorder* (Cambridge University Press, Cambridge, 1979)
[42] D.C. Elias et al., Science 323, 610 (2009); Nat. Mater. 8, 163 (2009)
[43] A. Peigney, C. Laurent, E. Flahaut. Carbon 2001, 39, 507 – 514.
[44] X. Du, I. Skachko, A. Barker. Nat. Nanotechnol. 2008, 3, 491 – 495.
[45] M. Dragoman, D. Dragoman, Prog. Quantum Electron. 2009, 33, 165 – 214.
[46] A. A. Balandin, S. Ghosh, W. Bao, I. Calizo, D. Teweldebrhan, F. Miao, C. N. Lau, Nano Lett. 2008, 8, 902 – 907.
[47] C. Lee, X. Wei, J. W. Kysar, J. Home, Science 2008, 321, 385 – 388.

[48] R. R. Nair, P. Blake, A. N. Grigorenko, K. S. Novoselov, T. J. Booth, T.
[49] Sungjin Park. Nano Letters 2009. 9, 4 (1593-1597).
[50] Muszynski, R. *J. Phys. Chem. C* 2008, *112*, 5263–5266.
[51] Li, D.; Muller. *Nat. Nanotechnol.* 2008, *3*, 101–105.
[52] Williams, G. *ACS Nano* 2008, *2*, 1487– 1491.
[53] Tung, V. C. *Nat. Nanotechnol*. 2009, *4*, 25 - 29.
[54] Stankovich, S. *Carbon* 2007, *45*.
[55] Wang, G. *J. Phys. Chem. C* 2008, *112*, 8192 – 8195.
[56] McAllister, M. J.A. *Chem. Mater.* 2007, *19*, 4396 – 4404.
[57] Schniepp, H. C.; Li, J.-L. *J. Phys. Chem. B* 2006, *110*, 8535 – 8539.
[58] C. Goh, M. D. McGehee, The Bridge 2005, 34, 33 – 39.
[59] N. S. Lewis, MRS Bull. 2007, 32, 808 – 820.
[60] T. W. Hamann, R. A. Jensen, A. B. F. Martinson, H. V. Ryswyk, J. T. Hupp, Energy Environ. Sci. 2008, 1, 66 – 78.
[61] R. L. Hirsch, Energy Policy 2008, 36, 881 – 889.
[62] G. F. Brown, J. Wu, Laser Photonics Rev. 2009, 3, 394 – 405.
[63] L. L. Kazmerski, M. S. Ayyagari, F. R. White, G. A. Sanborn, J. Vac. Sci. Technol. 1976, 13, 139– 144.
[64] J. Brown, C. W. Bates, Jr., J. Appl. Phys. 1990, 68, 2517 – 2519.
[65] K. J. Hong, T. S. Jeong, C. J. Youn, J. Appl. Phys. 2006, 100, 123518.
[66] W. K. Metzger, M. Gloeckler, J. Appl. Phys. 2005, 98, 063701.
[67] G. F. Brown, J. Wu, Laser Photonics Rev. 2009, 3, 394 – 405.
[68] N. Yang, J. Zhai, D. Wang, Y. Chen, L. Jiang, ACS Nano 2010, 4, 887 – 894.
[69] L. Hu, D. S. Hecht, G. Gruner, Nano Lett. 2004, 4, 2513 – 2517.
[70] Z. C. Wu, Z. H. Chen, X. Du, J. M. Logan, J. Sippel, M. Nikolou, K. Kamaras, J. R. Reynolds, D. B. Tanner, A. F. Hebard, A. G. Rinzler, Science 2004, 305, 1273 –1276.
[71] M. Rowell, M. A. Topinka, M. D. McGehee, H. Prall, G. Dennler, N. S. Sariciftci, L. Hu, G. Gruner, Appl. Phys. Lett. 2006, 86, 233506.
[72] S. Barazzouk, S. Hotchandani, K. Vinodgopal, P. V. Kamat, J. Phys. Chem. B 2004, 108, 17015 – 17018.
[73] R. R. Nair, P. Blake, A. N. Grigorenko, K. S. Novoselov, T. J. Booth, T. Stauber, N. M. R. Peres, A. K. Geim, Science 2008, 320, 1308 –1308.
[74] S. Stankovich, D. A. Dikin, G. H. B. Dommett, K. M. Kohlhaas, E. J. Zimney, E. A. Stach, R. D. Piner, S. T. Nguyen, R. S. Ruoff, Nature 2006, 442, 282 – 286
[75] Donner, S.; Li, H. W.; Yeung, E. S.; Porter, M. D. Fabrication of Optically Transparent Carbon Electrodes by the Pyrolysis of Photoresist Films: Approach to Single- Molecule Spectroelectrochemistry. *Anal. Chem.* 2006, *78*, 2816–2822.
[76] Héctor A. Becerril, Jie Mao, Zunfeng Liu. Evaluation of Solution-Processed Reduced Graphene Oxide Films as Transparent Conductors. ACS Nano VOL. 2 NO. 3 463 – 470 (2008).
[77] Wilson NR, Pandey PA, Beanland R, Young RJ, Kinloch IA, Gong L, et al. Graphene oxide: structural analysis and application as a highly transparent support for electron microscopy. ACS Nano 2009;3:2547
[78] Li D, Muller MB, Gilje S, Kaner RB, Wallace GG. Processable aqueous dispersions of graphene nanosheets. Nat Nanotechnol 2008;3:101.
[79] Park, S.; An, JH; Jung, IW; Piner, RD; An, SJ; Li, XS; Velamakanni, A.; Ruoff, RS Colloidal Suspensions of Highly Reduced Graphene Oxide in a Wide Variety of Organic Solvents Nano Lett. 2009, 9, 1593 – 1597.
[80] T. Rattanaa, S.Chaiyakun. Preparation and characterization of graphene oxide Nanosheets. Pocedia Engineering 32 (2012) 759 - 764
[81] Haiqing Hu, Yin Liu. A study on the preparation of highly conductive graphene. Materials Letters 65 (2011) 2582 – 2584.
[82] Zongrong Ying, Xuemei Lin. Preparation and characterization of low-temperature expandable graphite. Materials Research Bulletin. Volume 43, Issue 10, 2 October 2008, Pages 2677–2686

[83] Wang G, Yang Z, Li X, Li C. Synthesis of poly(aniline-co-oanisidine)- intercalated graphite oxide composite by delamination/ reassembling method. Carbon 2005;43(12):2564 – 70.
[84] Lerf A, He H, Forster M, Klinowski J. Structure of graphite oxide revisited. J Phys Chem B 1998;102(23):4477 – 82.
[85] S. Stankovich, Dmitriy A. Dikin. Synthesis of graphene-based nanosheets via chemical reduction of exfoliated graphite oxide. Carbon 45 (2007) 1558 – 1565
[86] Gratzel, M. Photoelectrochemical cells. *Nature* 414, 338 – 344 (2001).
[87] Hagfeldt, A. & Gratzel, M. Molecular photovoltaics. *Acc. Chem. Rec.* 33, 269 – 277 (2000).
[88] Ardo, S. & Meyer, G. J. Photodriven heterogeneous charge transfer with transition-metal compounds anchored to TiO_2 semiconductor surfaces. *Chem. Soc. Rev.* 38, 115 – 164 (2009).
[89] Hagfeldt, A., Boschloo, G., Sun, L., Kloo, L. & Pettersson, H. Dye-sensitized solar cells. *Chem. Rev.* 110, 6595 – 6663 (2010).
[90] O'Regan, B. & Gratzel, M. A low-cost, high-efficiency solar cell based on dye sensitized colloidal TiO_2 films. *Nature* 353, 737 – 740 (1991).
[91] Green, M. A., Emery, K., Hishikawa, Y., Warta, W. & Dunlop, E. D. Solar cell efficiency tables (version 38). *Prog. Photovolt. Res. Appl.* 19, 565 – 572 (2011).
[92] Ito, S. *et al.* Fabrication of thin film dye sensitized solar cells with solar to electric power conversion efficiency over 10%. *Thin Solid Films* 516, 4613 – 4619 (2008).
[93] Robertson, N. Optimizing dyes for dye-sensitized solar cells. *Angew. Chem. Int. Ed.* 45, 2338 – 2345 (2006).
[94] Mishra, A., Fischer, M. K. R. & Bauerle, P. Metal-free organic dyes for dye sensitized solar cells: From structure–property relationships to design rules. *Angew. Chem. Int. Ed.* 48, 2474 – 2499 (2009).
[95] Oskam, G., Bergeron, B. V., Meyer, G. J. & Searson, P. C. Pseudohalogens for dye-sensitized TiO_2 photoelectrochemical cells. *J. Phys. Chem. B* 105, 6867 – 6873 (2001).
[96] Nusbaumer, H., Moser, J.-E., Zakeeruddin, S. M., Nazeeruddin, M. K. & Gratzel, M. $Co^{II}(dbbip)_2^{2+}$ complex rivals tri-iodide/iodide redox mediator in dye-sensitized photovoltaic cells. *J. Phys. Chem. B* 105, 10461 – 10464 (2001).
[97] Zhang, Z., Chen, P., Murakami, T. N., Zakeeruddin, S. M. & Gratzel, M. The 2,2,6,6-tetramethyl-1-piperidinyloxy radical: An efficient, iodine-free redox mediator for dye-sensitized solar cells. *Adv. Funct. Mater.* 18, 341 – 346 (2008).
[98] Wang, P., Zakeeruddin, S. M., Moser, J.-E., Humphry-Baker, R. & Gratzel, M. A solvent-free, $SeCN^-/(SeCN)_3^-$ based ionic liquid electrolyte for highefficiency dye-sensitized nanocrystalline solar cells. *J. Am. Chem. Soc.* 126, 7164 – 7165 (2004).
[99] Hattori, S., Wada, Y., Yanagida, S. & Fukuzumi, S. Blue copper model complexes with distorted tetragonal geometry acting as effective electron transfer mediators in dye-sensitized solar cells. *Jpn. J. Appl. Phys.* 127, 9648 – 9654 (2005).
[100] Nazeeruddin, M. K. *et al.* Combined experimental and DFT–TDDFT computational study of photoelectrochemical cell ruthenium sensitizers. *J. Am. Chem. Soc.* 127, 16835 – 16847 (2005).
[101] Gao, F. *et al.* Enhance the optical absorptivity of nanocrystalline TiO_2 film with high molar extinction coefficient ruthenium sensitizers for high performance dye-sensitized solar cells. *J. Am. Chem. Soc.* 130, 10720 – 10728 (2008).
[102] Chen, C.Y. *et al.* Highly efficient light-harvesting ruthenium sensitizer for thin-film dye-sensitized solar cells. *ACS Nano* 3, 3103 – 3109 (2009).
[103] Chiba, Y. *et al.* Dye-sensitized solar cells with conversion efficiency of 11.1%. *Jpn. J. Appl. Phys.* 45, 638–640 (2006).
[104] Huang, S., Schlichthorl, G., Nozik, A., Gratzel, M. & Frank, A. Charge recombination in dye-sensitized nanocrystalline TiO_2 solar cells. *J. Phys. Chem. B* 101, 2576 – 2582 (1997).

[105] Boschloo, G. & Hagfeldt, A. Characteristics of the iodide/triiodide redox mediator in dye-sensitized solar cells. *Acc. Chem. Rec.* 42, 1819 – 1826 (2009).
[106] Bisquert, J., Fabregat-Santiago, F., Mora-Seró, I. N., Garcia-Belmonte, G. & Giménez, S. Electron lifetime in dye-sensitized solar cells: Theory and interpretation of measurements. *J. Phys. Chem. C* 113, 17278 – 17290 (2009).

Annexes

1. I-V curve characteristic

1.1 PV parameters

In particular, solar cells have a number of mechanisms that will capture slow-moving electrons of low energy (voltage). Under normal conditions in bright sunlight, these effects are saturated and represent a fixed loss in energy terms. However, at lower insolation levels (overcast day), these mechanisms represent an increasing percentage of the total power being generated. It is also common for cells to be saturated if there is too much insolation, and the number of free electrons or their mobility is too small. For instance, in silicon the holes left by the photoelectrons take some time to be neutralized, and during this time they can absorb a photoelectron from another atom within the cell. This leads to maximum production rates as well as minimum.

If a cell was free of these effects, the graph between voltage, current and output power would form a rectangle on a graph of current vs. voltage. In practice, the actual output is non-linear. V_{oc}, and I_{sc} are enough information to give a useful approximate model of the electrical behavior of a photovoltaic cell under typical conditions.

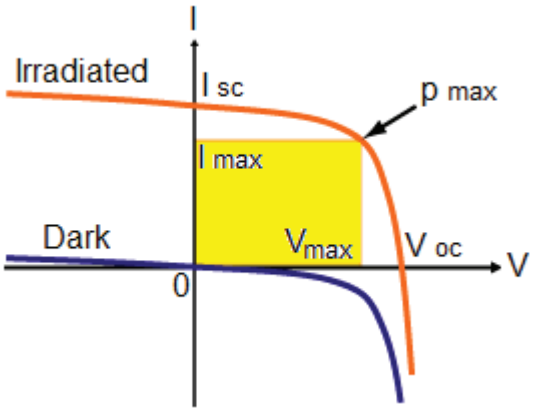

Annexes Figure 1. The IV-curve of a solar cell at a particular light level, and in darkness. The yellow area is the maximum power able to be drawn from this cell. The area formed between I_{sc} and V_{oc} and the yellow line returns the fill factor.

A current-voltage I-V curve shows the possible combinations of current and voltage output of a photovoltaic PV device (annexes figure 1). A photovoltaic device, such as a solar cell, produces its maximum current when there is no resistance in the circuit, i.e., when there is a short circuit between its positive and negative terminals. This maximum current is known as the short circuit current and is abbreviated I_{sc}. When the module is shorted, the voltage in the circuit is zero.

Conversely, the maximum voltage occurs when there is a break in the circuit. This is called the open circuit voltage V_{oc}. Under this condition the resistance is infinitely high and there is no current, since the circuit is incomplete.

These two extremes in load resistance, and the whole range of conditions in between them, are depicted on the I-V curve. Current, expressed in amps, is on the (vertical) y-axis. Voltage, in volts, is on the (horizontal) x-axis.

The power available from a photovoltaic device at any point along the curve is just the product of current and voltage at that point and is expressed in watts. At the short circuit current point, the power output is zero, since the voltage is zero. At the open circuit voltage point, the power output is also zero, but this time it is because the current is zero.

1.2 **Solar cell efficiency**

Is the ratio of the electrical output of a solar cell to the incident energy in the form of sunlight. The energy conversion efficiency (η) of a solar cell is the percentage of the solar energy to which the cell is exposed that is converted into electrical energy. This is calculated by dividing the power cell output (in watts) at its maximum power point (P_m) by the input light (E, in W/m^2) and the surface area of the solar cell (A_c in m^2).

$$\eta = \frac{P_m}{E \times A_c}$$

By convention, solar cell efficiencies are measured under standard test conditions (STC) unless stated otherwise. STC specifies a temperature of 25 °C and an irradiance of 1000 W/m^2 with an air mass 1.5 (AM1.5) spectrum.